E-cadherin-dependent phosphorylation of EGFR governs a homeostatic feedback loop controlling intercellular junction viscosity and collective migration modes.

Chaoyu Fu [1], Florian Dilasser [1*], Shao-Zhen Lin[2*], Marc Karnat[2*], Aditya Arora[1], Harini Rajendiran[1], Hui Ting Ong[1], Nai Mui Hoon Brenda[3], Sound Wai Phow[1], Tsuyoshi Hirashima[1], Michael Sheetz [1], Jean-François Rupprecht[2*], Sham Tlili [3*], Virgile Viasnoff [1,4]

Affiliations:

[1] Mechanobiology Institute, National University of Singapore, 5a engineering drive 1 117411 Singapore.

[2] Aix Marseille Univ, Université de Toulon, CNRS, CPT (UMR 7332), Turing Centre for Living systems, Marseille, France.

[3] Department of Biomedical Engineering, National University of Singapore, 4 Engineering Drive 3, 117583, Singapore.

[4] Aix Marseille Univ, IBDM (UMR 7288), Turing Centre for Living systems, Marseille, France.

[5] CNRS IRL 3639, 5a Engineering drive 1, 117411 Singapore.

[*] Equally contributed

Corresponding author: virgile.viasnoff@cnrs.fr

Abstract:

Actomyosin tension has been shown to be a ubiquitous driver of tissue morphogenesis[1, 2]. The Rho pathway, a prominent regulatory network influencing cortical tension, plays a central role in both tissue reorganisation and cell migration[3-6]. While viscous dissipation in the actin network is commonly regarded as a constant passive parameter in cell migration in both 2D and 3D contexts, there is limited knowledge concerning the regulation of dissipative forces arising from viscous drag between cells during collective rearrangement. Here, we found that the phosphorylation of Epithelial Growth Factor Receptor (EGFR) downstream of *de novo* E-cadherin adhesion[7, 8] orchestrates a feedback loop, thereby governing intercellular viscosity via the Rac pathway regulating actin dynamics. Our findings highlight how the E-cadherin-dependent EGFR activity controls the migration mode of collective cell movements independently of intercellular tension. Combining molecular cell biology, micropatterning, and *in silico* simulation, our work suggests the existence of a regulatory loop by which cells can tune junctional actin viscosity, with implications for the phenomenology of morphogenetic movements.

Main.

We postulated the existence of a feedback loop between cell junction elongation and E-cadherin-dependent phosphorylation of EGFR at junctions. This hypothesis was tested on Madin-Darby Canine Kidney (MDCK) cells with 2D migration in a culture dish. All experiments were conducted using both serum-free and serum-rich media, with consistently similar phenotypes observed, albeit more pronounced effects in serum-free conditions. All presented results pertain to serum-free conditions (**Methods**).

We first compared the migration of MDCK cells under control conditions and following selective inhibition of EGFR phosphorylation using Erlotinib at 1µM. Quantification of cell movement on 2D or 1D line patterns (**Extended Data Fig. 1a, c**) demonstrated that the migration of single isolated cells remained insensitive to EGFR inhibition. Consequently, we ruled out the possibility that EGFR inhibition directly altered cell-substrate interactions as well as their single cell migration potential. In contrast, EGFR inhibition significantly impacted collective cell migration on 2D sparse islets and 1D line patterns (**Fig. 1a, Extended Data Fig. 1b, d, and Supplementary Video 1**). In the former case, EGFR inhibition markedly reduced the cellular swirling motion of cells by inhibiting EGFR phosphorylation. The velocity at which each contact changes length during migration (**Methods**), exhibited a 2-fold decrease upon inhibition (**Fig. 1b**). Thus, EGFR dephosphorylation reduced the dynamics of cell junction deformation.

Reciprocally, we impeded the physical deformation of contacts during migration by supplementing the medium with 50 µg/mL of dextran (5, 50 and 270 kDa) to increase the medium viscosity. We carefully ensured that the addition of dextran induced minimal osmotic shock (**Extended Data Fig. 2a**). In media with higher viscosity (270kDa dextran), the migration speed of individual isolated cells decreased by 28 % (**Extended Data Fig. 2b**). Within cohesive patches consisting of 20 to 50 cells, both collective migration and contact deformation ceased within 10 minutes of adding 50 µg/mL dextran (**Fig. 1c, Extended Data Fig. 2c and Supplementary Video 2**). The individual cell velocity within the patch decreased from 13.7 ±

48   0.13 μm/h (N=1735 cells) in the control group to 8.2 ± 0.06 μm/h (N=1925) for 270kDa
49   dextran. Immunostaining revealed a significant reduction in the phosphorylation of EGFR at
50   the apical junction (**Extended Data Fig. 2d**). Western blots confirmed a 75% reduction in the
51   phosphorylation of the Src-dependent site Y845 pEGFR[9], while the other phosphorylation
52   sites (Y1068, Y1173) remained inactive under serum-free conditions (**Fig. 1d**). Our data
53   strongly suggest that the physical arrest of cell junction deformation directly or indirectly
54   leads to the dephosphorylation of apical pEGFR at its Src-dependent site.
55
56   We subsequently investigated whether enhancing pEGFR would favour the dynamics of
57   contact deformation. To do so, we transfected MDCK cells with EGFR coupled to the RUSH
58   system (**Methods**). The RUSH-EGFR construct was sequestered on the ER membrane until
59   released by biotin addition in the culture medium[10]. We established a high-confluence, non-
60   polarised (95%) MDCK monolayer, resulting in a mosaic expression of RUSH-EGFR, with small
61   patches of positive cells amid non-expressing control MDCK cells (**Fig. 1e**). Prior to the
62   addition of biotin, the cells displayed limited junctional localization and weak recruitment of
63   apical EGFR (**Supplementary Video 3**). Upon the addition of biotin, the RUSH-positive cells
64   showed a substantial recruitment of EGFR at the cell contacts, leading to a 5-fold increase
65   (from 2.6 ± 0.5 to 14.3 ± 1.2 μm/h) in their junction elongation velocity, quantified using
66   Cellpose neural network segmentation of the cell contours (**Fig. 1e, f and Methods**). In RUSH-
67   positive cells, EGFR localized exclusively to cell-cell contacts within minutes (**Extended Data
68   Fig. 3a**). To validate these findings, we repeated the experiment in the presence of Erlotinib
69   (1μM). Despite the relocalization of EGFR to the junctions (**Extended Data Fig. 3b and
70   Supplementary Video3**), the junction elongation velocity remained as low as the control, with
71   very limited cellular rearrangements. These results strongly suggest that the burst increase in
72   pEGFR at cell-cell contacts favours the dynamics of contact deformation.
73
74   Conversely, we induced the physical elongation of cell junctions by embedding obstacles
75   (non-adhesive disks with a diameter of 200μm, **Methods**) into high confluence monolayers
76   (**Fig. 1g**). Only the limited number of cell layers that spontaneously elongated and encircled
77   the obstacles displayed deforming junctions (**Fig. 1g and Supplementary Video 4**) and
78   elevated levels of apical pEGFR (**Fig. 1g**), in sharp contrast to the immobile bulk cells (**Fig. 1h**).
79   A treatment with Erlotinib inhibited the elongation and circumrotation of the cells around the
80   obstacle (**Supplementary Video 4**). Taken together, our findings support the hypothesis of a
81   positive feedback loop (**Fig. 1i**) between apical EGFR phosphorylation and junction elongation.
82   We subsequently delved into the molecular mechanisms underlying this phenomenon.
83
84   The absence of the soluble ligand EGF and the specific phosphorylation of Y845 suggested an
85   E-cadherin (Ecad)-dependent activation of EGFR[7, 8, 11]. Confluent patches of WT-MDCK cells
86   displayed a two-fold decrease in apical pEGFR compared to sub-confluent patches (27.6 ±
87   11.1 A.U. vs 51.6 ± 19.0 A.U.) (**Fig. 2a**). In contrast, Ecad-KO tissues showed consistently low
88   levels of apical pEGFR in both confluent and sub-confluent cases (4.0 ± 2.3 A.U. vs 6.1 ± 3.2
89   A.U.), while still forming cohesive patches (likely due to K-cadherins, quantified in (**Extended
90   Data Fig. 4c**) with a proper junctional actin structure. In Ecad-KO MDCK cells with rescued
91   expression of Ecad (Ecad-Res), the pEGFR levels in confluent and sub-confluent tissues
92   returned to their control values (22.2 ± 4.0 A.U. vs 30.2 ± 7.9 A.U.). Furthermore, when EGFR
93   was inhibited by adding Erlotinib (1 μM), the apical pEGFR for both confluent and sub-

94 confluent patches in WT-MDCK, Ecad-KO MDCK, and Ecad-Res MDCK all dropped to low levels
95 (**Extended Data Fig. 4a, b**).
96
97 We further validated the direct phosphorylation of EGFR at adherens junctions. We used Total
98 Internal Reflection Fluorescence (TIRF) microscopy to image the live recruitment of cytosolic
99 SH2-Grb2 to the membrane as a proxy for EGFR phosphorylation[12]. MDCK cells stably
100 expressing tdEOS-labelled SH2-Grb2 were left to spread on E-Cad coated circular patterns
101 (25µm diameter) (**Fig. 2b and Methods**). SH2-Grb2 dynamically accumulated in elongated
102 structures that dynamically followed the progression of cell edges with a time delay Δt. A
103 parallel experiment using E-cad-GFP MDCK cells revealed a similar accumulation of E-cad in
104 structures with similar time delay Δt (1.3 ± 0.2 min for E-cad-GFP, 1.5 ± 0.2 min for SH2-Grb2)
105 (**Fig. 2b**). Our findings imply that the engagement of E-cad during junction elongation results
106 in transient phosphorylation of EGFR. Consequently, the arrest of cell junction elongation
107 leads to the dephosphorylation of pEGFR, whereas its physical induction promotes EGFR
108 phosphorylation.
109
110 We then scrutinized the alteration of recruitment of actin regulators in the same conditions
111 as above. EGFR phosphorylation is a major regulator of Erk, a kinase extensively implicated in
112 collective cell migration mechanisms[13]. Monitoring Erk activity using Fluorescence Resonance
113 Energy Transfer (FRET) did not reveal any changes following the addition of 50µg/mL dextran
114 to migrating cells (**Extended Data Fig. 5a**). This suggests that Erk signaling is not downstream
115 of EGFR in our experimental context. To further dissect the molecular events, we performed
116 pulldown assays to gauge the activity of Rho family GTPases, which are key regulators of actin
117 dynamics[14]. The introduction of dextran to migrating cells resulted in a 28.9% reduction in
118 Rac1 activity, with no discernible effects on Cdc42 and RhoA (**Fig. 2c**). However, the broad
119 nature of pulldown assays made it challenging to distinguish whether Rac1 activity was
120 junctional or lamellipodial. Notably, Wave2, a downstream target of Rac1, was present at the
121 apical side of the junction[15] (**Extended Data Fig. 5b**). Surprisingly, the recruitment of Wave2
122 and Arp2/3, two factors promoting branched actin nucleation, was higher in confluent
123 monolayers (58.0 ± 24.0 A.U. and 91.1 ± 18.8 A.U., respectively) than in sub-confluent patches
124 (43.9 ± 22.9 A.U. and 63.9 ± 11.9 A.U., respectively) , a difference that is substantially reduced
125 upon treatment with Erlotinib (1µM) (**Fig. 2d, e and Extended Data Fig. 5b, c**). The amount of
126 phosphorylated Myosin light chain (pMLC) remained unaffected by pEGFR both in confluent
127 and sub-confluent culture conditions (**Fig. 2f and Extended Data Fig. 5d**). Our data advocate
128 for a model wherein the trans binding of new E-cadherin in elongating junctions, increasing
129 the junctional level of pEGFR, subsequently activating Rac1, decreasing levels of Wave2 and
130 Arp2/3 with a constant myosin level, thereby establishing a balance between branched and
131 linear junctional actin. **Fig. 2g** illustrates this feedback homeostatic loop.
132
133 Next, we evaluated the impact of EGFR phosphorylation on the turnover rate of junction actin
134 using Fluorescence Recovery After Photobleaching (FRAP). We compared junctions in
135 confluent monolayers, cells surrounding obstacles, and sub-confluent patches with or without
136 EGFR inhibition (**Fig. 2h and Extended Data Fig. 6a-c**). In all cases, we observed a deceleration
137 in actin turnover when pEGFR levels were lower. Additionally, we probed junctional tension
138 by assessing fast actin recoil following laser ablation (**Fig. 2i**). We did not detect any
139 substantial difference, proving that pEGFR does not regulate tension in this specific context.
140 Finally, we probed the viscoelastic properties of junctions using Atomic Force Microscopy

141 (AFM), revealing an increase in the loss modulus upon EGFR inhibition, with no changes in the
142 elastic modulus (**Extended Data Fig. 6d-f**).
143
144 We previously reported that E-cad-dependent phosphorylation of EGFR in suspended cell
145 doublets increases the velocity of *de-novo* junction formation[8] and the toughness of their
146 adhesion[16]. In all cases, the microscopic dynamics of the actin cortex are associated with a
147 change in cell deformability, with minimal impact on cortical tension. This implies that the
148 homeostasis of junction viscosity is regulated by the Ecad-dependent EGFR phosphorylation
149 loop, effectively "self-lubricating" junction elongation.
150
151 By analogy with the transition from laminar to turbulent flows of fluids at various Reynolds
152 numbers, we monitored how the inhibition of EGFR alters patterns of collective MDCK
153 migration along fibronectin strips (width, 400 µm; length, 3000 µm) (**Methods**). **Fig. 3a** and
154 **Supplementary Video 5** show the leading region (0-500 µm from the front) of migrating cells
155 in ctrl and Erlotinib conditions over 12 hours. Although migration fronts collectively
156 progressed at similar velocities in both conditions, inhibition of pEGFR abolished the vortices
157 observed in the ctrl case, leading to more laminar flows with enhanced cellular elongation in
158 the direction of migration. We subsequently quantified these qualitative observations. The
159 high level of apical pEGFR in Ctrl was significantly reduced in the inhibitory case (**Fig. 3b**). In
160 the bulk regions (3 mm away from the front), the level of apical pEGFR remained constant in
161 both conditions. We computed the cellular flow lines in the monolayer (**Methods**) to
162 established maps of cell velocities and flow vorticity (**Fig. 3c, d**). Additionally, we used CellPose
163 to segment individual cells (**Methods**) and to quantify the individual level of strain on each
164 cell. pEGFR inhibition resulted in around a 3-fold increase in cellular strain (0.06 ± 0.04 in Ctrl,
165 0.14 ± 0.06 in Erlotinib; n=1060 cells) (**Fig. 3e**). While the collective velocity of the migration
166 fronts was not affected by pEGFR inhibition (15.0 ± 4.7 µm/h in Ctrl, 14.8 ± 2.9 µm/h in
167 Erlotinib; N=16 strips), it substantially reduced the individual cell velocity within the
168 monolayer (from 18.7 ± 2.0 µm/h to 12.6 ± 2.0 µm/h; n= 182 cells) (**Fig. 3g**). Likewise, the
169 vorticity of the collective flow (**Fig. 3h)** was reduced by 2-fold (0.70 ± 0.10 h^{-1} to 0.33 ± 0.05 h^{-1}
170 ; n= 182 cells), and the correlation length of the cell velocity increased by 2-folds
171 (**Supplementary Fig. 4**).
172
173 To further substantiate the hypothesis regarding a change in intercellular viscosity, we
174 inferred the average shape relaxation time t_{visc} of cells within the monolayer. This parameter
175 proved to be a reliable indicator of cellular viscoelasticity in migrating monolayers[17]. **Fig. 3i, j**
176 illustrates the analysis procedure. Initially, we segmented phase-contrast images of the
177 monolayer at a specific time point. Subsequently, we computed the average initial cell strain
178 on a coarse-grained grid (**Methods**) and used an optic flow method to estimate the flow lines
179 (**Methods**). The evolution of local cellular strain was then evaluated using the approach
180 depicted in **Fig. 3i** and elaborated on in the **Supplementary Information**. The only free
181 parameter in this equation is the intrinsic strain relaxation time t_{visc}, which does not depend
182 on the shear level experienced by the cells. By utilizing the strain map at t = 0 and solving the
183 equation along the flow lines, we inferred the final strain map at a later time point (10 h). We
184 varied t_{visc} to maximise the correlation between the observed and measured strain maps. The
185 best fits lead to t_{visc} = 75 ± 15 min (R^2=0.4±0.04; N=3) for the control group and t_{visc} = 210 ± 65
186 min (R^2=0.34±0.2; N=3) for the pEGFR inhibition group (**Fig. 3k, l**). In the control conditions,
187 cells exhibited shape relaxation when advected in swirling vortices, while under pEGFR

188   inhibitory conditions, they elongated more in directed laminar, plug-like flows
189   (**Supplementary Video 6).** As pEGFR inhibition did not affect the single-cell migration
190   (**Extended Data Fig. 1a, c**), the approximately 3-fold increase in cell shape relaxation times
191   supports the hypothesis that the level of pEGFR controls viscous dissipation in cell-cell
192   junction elongation.
193
194   Finally, we designed a vertex model with viscosity (**Supplementary Information**) to
195   demonstrate that a modulation of intercellular viscosity can account quantitatively for our
196   observations. In our model, the force balance at each tri-cellular junction is expressed as
197   follows:
198

199
$$\underbrace{\boldsymbol{F}_i^{\text{(elastic)}}}_{\text{elasticity}} + \underbrace{\boldsymbol{F}_i^{\text{(active)}}}_{\text{activity}} + \underbrace{\boldsymbol{F}_i^{\text{(friction)}}}_{\text{friction}} + \underbrace{\boldsymbol{F}_i^{\text{(viscous)}}}_{\text{viscosity}} = \boldsymbol{0}$$

200   The first 3 terms are standard for vertex models[18, 19] and correspond to: $\boldsymbol{F}_i^{\text{(elastic)}}$: the elastic
201   forces accounting for the mechanical regulation of the cell shape[20-23], that are assumed to
202   derive from a mechanical energy E :

203
$$E = \underbrace{\sum_J \frac{1}{2} K_A (A_J - A_0)^2}_{\text{area elasticity}} + \underbrace{\sum_J \frac{1}{2} K_P (P_J - P_0)^2}_{\text{perimeter elasticity}},$$

204   where the two terms account for the cell area elasticity and the cell perimeter elasticity,
205   respectively. In detail, K_A and K_P are the area stiffness and perimeter stiffness of cells,
206   respectively; A_J and P_J are the area and the perimeter of the J-th cell, respectively; A_0 and P_0
207   are the preferred area and preferred perimeter, respectively.
208    $\boldsymbol{F}_i^{\text{(active)}}$ corresponding to the active fluctuations of the cortical tension, assumed to be a
209   Gaussian white noise of amplitude Lambda (**Supplementary Information**), and

210
$$\boldsymbol{F}_i^{\text{(friction)}} = -\xi \boldsymbol{v}_i$$

211   corresponding to the friction of the cells on the underlying substrates.
212   We complemented this description by adding a viscous dissipation term accounting for
213   cortical deformation and cytoplasmic flows, which reads:

214
$$F_i^{\text{(viscous)}} = \sum_j \eta_{(i,j)} \ t_{(i,j)} \cdot (v_j - v_i) t_{(i,j)}$$

215   where $t_{(i,j)}$ is a unit vector oriented between the vertex i and j, which is either another vertex,
216   in which case $\eta_{(i,j)} = \eta^{(s)}$ is the viscous modulus dissipation along the cell surface (cortex), or
217   the cell barycenter, in which case $\eta_{(i,j)} = \eta^{(b)}$ is a viscous modulus, representing dissipation
218   within the cell bulk (cytoplasm) (details in the **Supplementary Information**).
219

220   First, we conducted simulations for the RUSH-EGFR experiment (**Fig. 1e, f**), considering a
221   down-step in intercellular viscosity on selected clusters of cells (N=4 cells) dispersed in a cell
222   monolayer at equilibrium (**Fig. 4a and Supplementary Information**). We used a set of
223   parameters summarised in **Supplementary Table I**, which were optimised to quantitatively
224   reproduce the experimental results, while remaining within the typical range used to describe
225   MDCK monolayers. In the simulations, a 10-fold decrease (from η=1.4 nN.min.μm^{-1} (30 a.u)
226   to η=0.14 nN.min.μm^{-1} (3 a.u)) in intercellular viscosity leads to a 4-fold increase (from 2.6 ±
227   0.1 to 10.6 ± 3.7 μm/h; N=100) in the junction elongation velocity (**Fig. 4b, c and**

228 **Supplementary Video 7**), aligning closely with the experimental values (from 2.6 ± 0.5 to 14.3
229 ± 1.2 μm/h) (**Fig. 1f**).
230

231 Second, we conducted simulations of collective cell migration along the strips (details in
232 **Supplementary Information**). We maintained the same set of parameters while introducing
233 additional conditions: (1) we posited that the inhibition of EGFR by Erlotinib leads to
234 intracellular viscosity equivalent to its downregulation in dense monolayers, given their
235 comparable recruitment levels. We hence set it to η= 1.4 nN.min.μm^{-1} (30 a.u) and (2) we
236 imposed the velocity of the migration front to align with experimental values of 15 μm/h (**Fig.**
237 **3g**). Subsequently, we tuned the intercellular viscosity of the Ctrl case to match the
238 experimental results, finding that η= 0.28 nN.min.μm^{-1} (6 a.u) yielded the best quantitative
239 predictions. The **Supplementary Video 7** shows a typical simulation output **(Fig. 4d-f)**. Both
240 experimental and simulated data underwent analysis using the same scheme. Notably, a
241 sizeable increase in cell strain (**Fig. 4g**), a decrease in cell velocity (**Fig. 4h**), a reduction in
242 vorticity (**Fig. 4i**), an expansion in spatial correlation length (**Supplementary Fig. 4**), as well as
243 an elevation in cell shape relaxation times t_{visc} (**Fig. 4j, k**) were observed between η= 0.28
244 nN.min.μm^{-1} (6 a.u) au (Ctrl) and η= 1.4 nN.min.μm^{-1} (30 a.u) (Erlotinib). These quantitative
245 findings closely matched the experimental observations (**Fig. 4l**).

246 In conclusion, we propose that the E-cadherin-dependent phosphorylation of EGFR fine-tunes
247 the structure of junctional actin, thereby affecting actin dynamics. On a larger scale, it
248 influences junctional viscosity, governing the collective modes of cell migration (**Fig. 2g**). This
249 insight demonstrates that E-cadherin-dependent EGFR activity could regulate the dynamics
250 of collective cell behavior and sheds light on the role of cellular viscous dissipation in collective
251 cell migration, an important aspect that has been understudied.

252

Methods

Cell culture and reagents

MDCK strain II cells were cultured at 37°C with 5% CO_2 in high-glucose Dulbecco's Modified Eagle Medium (DMEM, Invitrogen). The medium was supplemented with 10% fetal bovine serum (FBS, Invitrogen), and 100 units/mL of penicillin and 100 µg/mL of streptomycin (Pen-strep, Invitrogen).

To investigate collective migration behaviours, we utilised stable cell lines expressing fluorescent markers or knockout variants of MDCK cells. The following cell lines were employed: wild-type MDCK (MDCK-WT), stably transfected GFP–actin MDCK (MDCK-actin-GFP), stably transfected GFP–E-cadherin MDCK (MDCK-E-cad-GFP) (kindly provided by W. J. Nelson), histone-1–stable GFP MDCK (MDCK-H1-GFP), E-cad KO MDCK (MDCK-Ecad KO) (kindly provided by B. Ladoux, Institut Jacques Monod), and E-cad Rescue MDCK (MDCK-Ecad Res) (kindly provided by P. Kanchanawong, Mechanobiology Institute).

For serum starvation experiments, cells were subjected to serum starvation by incubating them in a growth medium. This medium consisted of high-glucose DMEM lacking FBS, supplemented with 100 units/mL of penicillin and 100 µg/mL of streptomycin. To inhibit EGFR activity, Erlotinib hydrochloride (1µM, Sigma-Aldrich) was employed.

Plasmids and transfection

The Str-KDEL_SBP-EGFP-EGFR plasmid was generously provided by Dr. David Marc Virshup's laboratory at Duke NUS. The "SH2-GRB2-tdEOS" plasmid was kindly gifted by Dr. Jay T Groves' Lab. MDCK-WT cells, with 80% confluence, were transfected with 3 µg of DNA using the Neon electroporation system (Invitrogen), following the manufacturer's instructions. For Erk activity measurement, EKAREV-NLS expressing MDCK cells were a kind gift from Dr. Tsuyoshi Hirashima's Laboratory at Mechanobiology Institute, NUS.

Stamp preparation for collective cell migration on line-patterned strips

Master molds featuring the desired pattern were crafted using SU8-3050 resist on silicon wafers through standard lithography techniques. The pattern employed in this study encompasses a sizable rectangular "reservoir" (approximately 5000 x 700 µm), interconnected with 10 rectangular strips (around 3000 x 400 µm each)[24]. Subsequently, Polydimethylsiloxane (PDMS) stamps were derived from these wafers and utilised for microcontact printing.

The PDMS stamps were incubated with Fibronectin (50µg/ml, Merck) for a duration of 45 minutes, after which they were transferred onto a 35 mm uncoated imaging dish (Ibidi) via microcontact printing. Prior to Fibronectin stamping, the dish had been pre-coated with a layer of PDMS and exposed to UV light for activation. The PDMS stamps were then air-dried within a laminar hood for 10 minutes and delicately pressed against the dish's bottom for 1

291 minute. Following microcontact printing, the PDMS stamps were carefully lifted without
292 causing any agitation. The dish bearing the Fibronectin-stamped pattern underwent
293 additional passivation by treating it with a 2% Pluronic F127 solution (Sigma) for 1 hour, aimed
294 at preventing cells from attaching and proliferating in the unstamped areas. Subsequent to
295 passivation, the dishes underwent thorough rinsing with PBS on three times. A PDMS block
296 was strategically positioned atop the microcontact-printed pattern, effectively confining cells
297 within the "reservoir" region. MDCK-H1-GFP, MDCK-Ecad KO, or MDCK-Ecad Res cells were
298 pre-treated with Mitomycin C at a concentration of 10µg/ml (Roche) for a duration of 1 hour
299 to inhibit cell proliferation. These MDCK cells were trypsinised and strategically seeded along
300 the periphery of the PDMS block to cover the "reservoir" area. Once the cells reached
301 confluence on the PDMS block's sides, the block was gently released, enabling cells to migrate
302 along the strips. Migrating cells were subsequently subjected to specific inhibitors as
303 indicated. The process of live imaging was executed using widefield microscopy (Olympus
304 IX81) with a 10x objective. Throughout imaging, the dishes were maintained within a
305 humidified environment at 37°C with 5% CO_2. Both phase-contrast and fluorescent images
306 were acquired at intervals of 4 minutes over a duration ranging from 12 to 24 hours.

307

Obstacle migration

309 The design employed for obstacle migration involves a substantial rectangular "reservoir"
310 (approximately 5000 x 700 µm), which is linked to 10 rectangular strips (around 3000 x 400µm
311 each). Each strip features a central circle with a diameter of 200µm. The PDMS stamps crafted
312 from these wafers encompass 200µm diameter circles within each strip. The subsequent
313 preparation steps remain consistent with those outlined in the preceding section. Following
314 contact printing and passivation, the 200µm diameter circles exhibit non-adhesive properties,
315 serving as obstacles during cell migration.

316

Single-cell without confinement, single-cell confined to lines, cell trains and cell patches migration

319 For the migration of single cell lines, wafers with a pattern of 20µm lines were utilised. PDMS
320 stamps were crafted from these wafers and subsequently employed for microcontact
321 printing. The preparation steps mirrored those outlined in the preceding section. Following
322 passivation, the dishes were primed for cell seeding. MDCK-H1-GFP or MDCK-WT cells were
323 trypsinised and their counts were determined prior to seeding. Approximately 4-5 x10^4 MDCK
324 cells were introduced into the imaging dish and allowed to incubate for 2 hours at 37 °C within
325 a 5% CO_2 incubator, facilitating full cellular spreading. The migrating cells were then subjected
326 to the indicated inhibitors.

327 For the migration of cell trains, the employed pattern comprises a large rectangular
328 "reservoir" (approximately 5000 x 700 µm), which is linked to 20 rectangular strips
329 (approximately 3000 x 20µm). The preparation steps mirror those outlined in the preceding
330 section for the creation of line-patterned strips. The migrating cells were subjected to
331 treatment using the specified inhibitors.

332   In the case of single-cell and cell patch migration, Fibronectin-coated dishes were utilised for
333   direct cell seeding. A quantity of 4-5 x 10^4 MDCK cells (for single cells) and 3-4 x 10^5 MDCK
334   cells (for cell patches) were seeded into the imaging dish and incubated at 37 °C within a 5%
335   CO_2 incubator for 2 hours to allow for complete cell spreading. The migrating cells were
336   subsequently treated with the indicated inhibitors.

337   Live imaging was conducted using widefield microscopy (Olympus IX81) with either a 10x or
338   20x objective. The dishes were positioned within a humidified chamber at 37 °C with 5% CO_2
339   during the imaging process. Phase-contrast and fluorescent images were captured at 10-
340   minute intervals, spanning a duration ranging from 12 to 24 hours. Migration speeds of
341   individual cells (n > 30) were tracked using either the TrackMate plugin for Image J on phase-
342   contrast images or Imaris for fluorescent nucleus images. The speed of junction deformation
343   at cell-cell junctions was quantified by measuring the lengths of these junctions at each time
344   point.

345

346   **Dextran experiments**

347   MDCK-H1-GFP cells (for live imaging) or MDCK-WT cells (for western blotting) were seeded at
348   a low confluence and subjected to overnight serum starvation. Subsequently, 50µg/mL of
349   dextran (00269, 00891, 00894, Sigma-Aldrich) with the specified molecular weight was
350   introduced to the cells before the execution of either western blotting or live imaging. The
351   latter was performed using a widefield microscopy setup (Olympus IX81) equipped with a 20x
352   objective. Cell velocity and confinement ratio were assessed using the Trackmate plugin
353   within Fiji.

354

355   **EGFR release experiment**

356   MDCK-WT cells were transfected with the RUSH plasmid Str-KDEL_SBP-EGFP-EGFR. Following
357   transfection, the cells were plated onto an Ibidi imaging dish pre-coated with Fibronectin and
358   placed in a complete medium at 37°C with 5% CO_2. Once the cells reached confluency,
359   overnight serum starvation was conducted. Subsequently, EGFR-GFP was liberated from the
360   endoplasmic reticulum (ER) through the addition of 40mM biotin. Live imaging was carried
361   out utilising a spinning-disc confocal microscope (Yokogawa CSU-W1) attached to a Nikon
362   Eclipse Ti-E inverted microscope body, equipped with a 60x NA1.3 water lens. Fluorescent
363   images were captured both prior to and subsequent to the biotin introduction, at 5-minute
364   intervals, spanning a duration of 6 hours. The speed of deformation at cell-cell junctions was
365   quantified by measuring the lengths of these junctions at each time point, both 30 minutes
366   before and 30 minutes after the release of EGFR. The measurements were then averaged over
367   this 30-minute period.

368

369   **Western blotting**

370 Cells were incubated on ice with RIPA lysis buffer (Sigma), supplemented with protease and
371 phosphatase inhibitor cocktails (Sigma). Subsequently, lysates underwent SDS-PAGE and
372 were transferred onto nitrocellulose membranes. The membranes were then blocked using
373 5% BSA and 0.05% Tween 20 in TBS, followed by incubation with the specified primary
374 antibodies. Detection of immune complexes was achieved using appropriate HRP-conjugated
375 secondary antibodies (Cell Signaling Technologies) and an enhanced chemiluminescence
376 reagent (Clarity ECL, BioRad). Protein band intensities were quantified using ImageJ Software.
377 The primary antibodies employed were pEGFRY845 (44784G, Thermo Fisher Scientific),
378 pEGFRY1068 (2234, Cell Signaling Technologies), pEGFRY1173 (4407, Cell Signaling
379 Technologies), EGFR (2232, Cell Signaling Technologies), RhoA (sc418, Santa Cruz), Cdc42
380 (ab187643, Abcam), Rac1 (610651, BD Biosciences) and β-actin (MA515739, Thermo Fisher
381 Scientific).

382 To assess Rho family GTPases activity, pull-down assay using GST-PBD and GST-RBD were
383 performed on cell lysates as described previously[25].

384

Immunofluorescence

386 After a collective cell migration period of 12-24 hours, MDCK cells were fixed using pre-
387 warmed 4% paraformaldehyde (PFA) in phosphate-buffered saline (PBS) at 37 °C for 15
388 minutes. Subsequently, they were permeabilised with 0.2% Triton X-100 in TBS for 30 minutes
389 at room temperature. Samples were then blocked using 1% BSA in TBS for 1 hour. The cells
390 were incubated overnight at 4 °C with primary antibodies: rabbit anti-phospho-EGFR (Y845)
391 polyclonal antibody (44-784G, Thermo Fisher Scientific, diluted 1:200); Purified Mouse anti-
392 E-Cadherin monoclonal antibody (Clone 36) (610181, BD Transduction Laboratories); WAVE2
393 antibody (H-110) (sc-33548, Santa Cruz); Arp3 antibody (A5979, Sigma-Aldrich); Phospho-
394 Myosin Light Chain 2 (Ser19) antibody (3671, Cell Signaling Technologies, diluted 1:50)
395 according to the manufacturer's instructions. Following three washes with PBS at 10-minute
396 intervals, cells were incubated with secondary antibodies (anti-mouse Alexa555-conjugated
397 secondary antibody and anti-Rabbit Alexa647-conjugated secondary antibody, both from
398 Thermo Fisher Scientific) along with Alexa405-coupled phalloidin (Invitrogen) in darkness at
399 room temperature for 1 hour. Subsequently, cells were rinsed with PBS and prepared for
400 imaging acquisition. Confocal images were captured in 3D stacks using a spinning-disc
401 confocal microscope (Yokogawa CSU-W1) mounted on a Nikon Eclipse Ti-E inverted
402 microscope body, equipped with a 100x NA1.5 or 60x NA1.3 lens.

403

Real-time quantitative PCR (qPCR)

405 The entire RNA was isolated from a single well of a 6-well plate using the RNeasy Plus Micro
406 Kit (QIAGEN), following the guidelines provided by the manufacturer. A quantity of 450ng of
407 total RNA was employed to generate the cDNA utilising the cDNA synthesis kit (SensiFAST™).
408 For qPCR analysis, the FastStart Universal SYBR Green Master (ROX) mix was employed on a
409 CFX96 Touch Real-Time PCR detection system (Bio-Rad). GAPDH was employed as the internal
410 reference gene.

411

Live cell spreading on E-cadherin-coated surface

413   Disks with a diameter of 25μm were photopatterned onto glass coverslips, following the
414   previously described method[26]. These patterns were then coated overnight at 4°C with a
415   recombinant E-cadherin Fc Tag protein (10204, Sino Biological) at a concentration of
416   20μg/mL, and subsequently gently washed with PBS. The patterned coverslips were mounted
417   within imaging chambers.

418   MDCK-WT cells were transfected with the SH2-GRB2-TdEos plasmid, and after selection with
419   500 μg/mL Geneticin (10131035, Thermo Fisher Scientific), a stable cell line was established
420   following sorting using an SH800S cell sorter (Sony). MDCK-SH2-GRB2-TdEos or MDCK-Ecad-
421   GFP cells were serum-starved overnight, then seeded onto Ecad-Fc patterns, and allowed to
422   spread for a period of 2 hours before initiating TIRF time-lapse imaging. This imaging was
423   carried out using a Motorised TIRF Module (Nikon) integrated with a Nikon Eclipse Ti-E
424   inverted microscope body.

425

Fluorescence recovery after photobleaching (FRAP)

427   Bleaching was performed on the actin of apical cell-cell junctions for FRAP measurements.
428   The cortical actin recovery time (t_{half}) was calculated by fitting the following exponential
429   function to the recovery curves:

$$I(t) - I(0) = \left(I\infty - I(0)\right)\left(1 - \exp\left(-ln2\frac{t}{t_{half}}\right)\right)$$

431

Laser ablation

433   An initial image was acquired to determine the precise laser spots. In the case of MDCK-actin-
434   GFP cells, the laser spots were positioned at the apical cell-cell junctions. The pre-acquisition
435   process involved capturing five images at 1-second intervals. During the acquisition phase, a
436   laser power of 60% was utilised, with a duration of approximately 1-2 seconds, targeting the
437   predetermined regions. Subsequently, the post-acquisition stage encompassed the capture
438   of 100 images at 1-second intervals.

439   To quantify the recoil velocity, the positions of two nodes within the defined junctions were
440   manually tracked using ImageJ software. Following the laser ablation, the temporal evolution
441   of the distance between these two nodes was fitted using a single exponential function. While
442   the double exponential function is commonly employed in other studies, it proved unsuitable
443   for our analysis. In our investigation, the recoil velocity exhibited a gradual nature, and fitting
444   it with a double exponential function yielded unrealistically high speeds. Consequently, we
445   opted to employ a single exponential function for a more appropriate representation.

446

Atomic force microscopy (AFM)

AFM experiments were conducted using a Nanowizard IV BioAFM system manufactured by JPK Instruments, Germany. Indentations were performed on randomly chosen cells at the junctional regions. This was achieved using a cantilever (with a nominal k value of 0.03 N/m, provided by Novascan Technologies, Inc., Ames, IA) with an attached polystyrene bead (4.5 μm diameter) at its tip. The applied force was set at 3 nN and a loading rate of 5 μm/s was used.

For each experimental condition, measurements were taken from over 30 cells across three independent trials and subsequently averaged. Young's modulus values were used to quantitatively describe the cellular stiffness. These values were calculated using the JPK Data Processing Software (JPK Instruments, Germany), which incorporates Hertz's contact model tailored to spherical indenters (with a diameter of 4.5 μm and a Poisson's ratio of 0.5). Energy dissipation, representing the heat-based loss of mechanical energy during each indentation cycle by the AFM tip, was determined by assessing the enclosed area between the approach and retraction curves (hysteresis). This phenomenon is largely attributed to frictional and viscous damping within the cell structure at this low speed[27].

Erk activity measurement

30000 EKAREV-NLS expressing cells were seeded into a well of culture-inserts 2 wells (81176, ibidi) and allowed to spread for 8 hours. Simultaneously, the insert was then removed and cells were serum starved overnight. Time-lapse FRET images were obtained using a Nikon AX point scanning confocal microscope mounted on a Ti-2 Nikon inverted body. To represent the FRET efficiency, FRET/CFP ratio images were generated after the background was substracted from the original images in the CFP and FRET channel using a matlab code kindly provided by Tsuyoshi Hirashima's Laboratory at Mechanobiology Institute, NUS. To quantify FRET Ratio for each cells at each timepoints, the Fiji Trackmate plugin was applied to the CFP channel to track each cell position overtime.

Segmentation

We used Cellpose[28] for the cell segmentation. We performed an erosion with a 3x3 square kernel to each mask to limit the occurrence of gaps between cells; we disregard objects with areas lower than 20 pixels. We define the cell inertia tensor, with a constant linear weight density along the segmented cell boundaries, i.e. with xx component $I_{xx} = \iint (x - \bar{x})^2 dxdy$, where $(\bar{x}, \bar{y})$ is the position of the cell barycenter. We call *average shape tensor* field the spatially and temporally averaged inertia matrix over all cells within 30x30 pixel-large boxes (corresponding to approx. 10 cells within each), regularly spaced on a spatial grid. The strain field is defined as $\epsilon = \log(\lambda_1/\lambda_2)/2$ where λ_1 (resp. λ_2) is the maximum (resp. minimum) eigenvalue of the average shape tensor. For the cell tracking, we used bTrack[29].

Simulation of EGFR release experiments

486

487 In our EGFR release experiments, cells under investigation are located in the bulk of the tissue,
488 far away from the boundary. In this case, we observe fluctuations in cell edge length but no
489 obvious cell motions, see **Fig. 1e**. To mimic such fluctuations in cell length, we here consider
490 active fluctuations of intercellular tension, $\Lambda_{ij}^{(\text{act})}$, at each cell-cell interface ij. These
491 fluctuations contribute to an active force at each vertex,

492
$$F_i^{(\text{active})} = \sum_{j \in \text{neighbor}} \Lambda_{ij}^{(\text{act})} \, t_{i,j},$$

493 where the summation is over all vertices that connect to the vertex i. We assume such tension
494 fluctuations satisfy an Ornstein-Uhlenbeck stochastic dynamic with time correlation[30],

495
$$\frac{\mathrm{d}\Lambda_{ij}^{(\text{act})}}{\mathrm{d}t} = -\frac{\Lambda_{ij}^{(\text{act})}}{\tau_\sigma} + \zeta_{ij}(t),$$

496 where τ_σ is the relaxation time of the active tension and $\zeta_{ij}(t)$ are independent Gaussian
497 white noises, satisfying $\langle \zeta_{ij}(t) \rangle = 0$ and $\langle \zeta_{ij}(t)\zeta_{kl}(t') \rangle = \Delta_\sigma^2 \delta_{ik}\delta_{jl}\delta(t - t')$ with Δ_σ being
498 the fluctuation intensity.

499 We simulated a cell sheet consisting of $N = 100$ cells in a square box of size $L = \sqrt{NA_0}$, using
500 periodic boundary conditions, see **Supplementary Fig. 1a**. We initialize our simulations from
501 a random Voronoi cell pattern and let the system relax toward a dynamic steady state where
502 the cell elongation parameter and cell motion velocity approach a steady plateau[22].

503 To model the effect of the light activation of EGFR and the possibility of a subsequent viscosity
504 modulation, we then randomly selected a small group of four cells in contact and decreased
505 the bulk viscosity $\eta_J^{(b)}$ of those four cells, from the default value (with $\eta_J^{(b)}(t < 0) = \eta^{(\text{CTL})}$)
506 to a lower value (with $\eta_J^{(b)}(t > 0) = \eta^{(\text{EGFR+})}$), see **Supplementary Fig. 1b**. Further, the
507 viscosity $\eta_{ij}^{(s)}$ along the cell-cell interface between the vertices i and j is assumed to be the
508 average viscosity of the two contacting cells (indexed by J and K) as $\eta_{ij}^{(s)} = \left(\eta_J^{(b)} + \eta_K^{(b)}\right)/2$.

509 We compare the junction remodeling velocity, $\dot{l}$, before and after the drop in viscosity. We
510 find that the ratio of the junction remodeling velocity $\dot{l}_{\text{after}}/\dot{l}_{\text{before}}$ increases with the ratio of
511 the cell viscosity decrease, $\eta^{(\text{CTL})}/\eta^{(\text{EGFR+})}$ (**Supplementary Fig. 2**). In particular, the data of
512 $\eta^{(\text{CTL})}/\eta^{(\text{EGFR+})} = 10$ agree with our experiments (**Supplementary Fig. 2**).

513 We provide the default parameter values for such simulations in **Supplementary Table I**.

514

515 **Simulation of collective cell migration experiments**

516 To simulate the collective cell migration experiments, we now turn to collective cells initially
517 confined in a rectangular geometry of size $L_x \times L_y$ with $L_x = 18\sqrt{A_0}$ and $L_y = 100\sqrt{A_0}$,
518 which contains around $N_{cell} \simeq 1800$ cells, see **Supplementary Fig. 3**.

519 As in the RUSH-EGFR model simulation, we first initialize the simulations using a Voronoi
520 tessellation. We then let the system relax, keeping the bottom boundary fixed and simulating
521 the cell sheet in a confined rectangular geometry to reach a steady state. We next relax the
522 bottom boundary and run the simulations to reach a dynamic steady state.

523 At the left, top, and right borders, cells are allowed to slip along but adhere to the boundaries;
524 while at the bottom boundary, we imposed vertices to move at a constant speed

525 $$v_y(\text{ bottom boundary vertices }) = -V_{front}, \quad v_x(\text{bottom boundary vertices }) = 0.$$

526 The value of V_{front} is fixed at a comparable value to the one measured in experiments.
527 Specifically, we set $V_{front} = 15\ \mu m/h$ in simulations.

528 With the sole migration at the edge (described above), we were not able to recapitulate the
529 formation of vortices similar to the one observed in experiments.

530 To recapitulate the formation of vortices similar to the one observed in experiments, we
531 turned to a Vicsek-like model of cell motility[23]. Within such model, we associate each cell with
532 an active force $\boldsymbol{F}_J^{(act)} = T_0(\cos\theta_J, \sin\theta_J)$ of magnitude T_0 and direction θ_J; such model
533 mimics the cell motility induced by cell protrusions[23], with the polar direction θ_J of each cell
534 J evolving according to the equation:

535 $$\frac{d\theta_J}{dt} = \frac{1}{n_J} \sum_{K \in \text{ neighbor}} \left\{ \mu_{LA}\sin\left[\theta_K^{(vel)} - \theta_J\right] + \mu_{CIL}\sin\left(\alpha_{J,K} - \theta_J\right) \right\} + \zeta_J(t)$$

536 where μ_{LA} and μ_{CIL} represent the strengths of local alignment interaction and contact
537 inhibition of locomotion, respectively; $\theta_K^{(vel)} = \arg(\boldsymbol{v}_K)$ refers to the argument angle of the
538 velocity $\boldsymbol{v}_K$ of cell K; $\alpha_{J,K} = \arg(\boldsymbol{r}_J - \boldsymbol{r}_K)$ denotes the argument angle of the vector pointing
539 from cell K to cell J; $\zeta_J(t)$ is a white-noise process with zero mean and variance $2D_r$. For the
540 cells at the free boundary, we constrain their polar active force direction θ_J to orient normally
541 to the free boundary and toward the free space.

542 To mimic cell flows from the top boundary (bulk region of MDCK cell sheet), we allow cell
543 divisions on a top region which is within a distance $d < 5$ cell length to the top boundary, see
544 **Supplementary Fig. 3**. We perform cell divisions once cells within such a region exceed an
545 area threshold $A_{div} = 1.5A_0 = 486\mu m^2$.

546 We provide the default parameter values for such simulations in **Supplementary Table II**.

547 We are interested in and examine the collective cell dynamics in a region near the moving
548 front (within a distance of ~ 30 cell length to the moving front). Note that to reduce the
549 artificial effect of the top boundary condition on collective cell migration dynamics in a region

550 near the moving front, we have set a sufficiently large scale of the simulated cell monolayer
551 in the vertical direction, i.e., $L_y \sim 100$ cell length.

552

Data display and statistics

554 Prism (GraphPad Software) and Matlab (Math Works) were used for data analysis and graph
555 plotting. Graphs were mounted using Adobe Illustrator. ANOVA test and paired or unpaired
556 Student's t-test were carried out to analyse the significant difference levels.

557

566

Author contributions:
568 Fu Chaoyu performed the migration experiments, their quantification and wrote the
569 manuscript. F. Dilasser performed the single cell experiments and the dextran experiment,
570 the pull-down assay. Zhao-zhen Lin performed all simulations. Marx Karnat did all the
571 segmentation and tracking, Sound Wai Phow and Tsuyoshi Hirashima helped with the ERK
572 experiments. Hui Ting Ong helped with image analysis. Nai Mui Hoon Brenda performed the
573 AFM experiments. Harini performed the QPCR, Aditya Arora contributed to the
574 understanding of the experimental results. Michael Sheetz initiated the work on EGFR and
575 supervised C.F. Jean-Francois Rupprecht supervised the simulation work and contributed to
576 the manuscript. Sham Tlili performed the relaxation time analysis and contributed to the
577 theoretical part of the work. Virgile Viasnoff designed the experiments, contributed to the
578 manuscript and supervised the work.

579

Conflict of Interest:
581 The authors declare no conflict of interest.

582

Reference:

584 1.   Martin, A.C., Kaschube, M. & Wieschaus, E.F. Pulsed contractions of an actin-myosin
585   network drive apical constriction. *Nature* **457**, 495-499 (2009).
586 2.   Bertet, C., Sulak, L. & Lecuit, T. Myosin-dependent junction remodelling controls
587   planar cell intercalation and axis elongation. *Nature* **429**, 667-671 (2004).
588 3.   Reffay, M. *et al.* Interplay of RhoA and mechanical forces in collective cell migration
589   driven by leader cells. *Nat Cell Biol* **16**, 217-223 (2014).

590 4. Ridley, A.J. Rho GTPase signalling in cell migration. *Curr Opin Cell Biol* **36**, 103-112
591   (2015).
592 5. Mason, F.M., Xie, S., Vasquez, C.G., Tworoger, M. & Martin, A.C. RhoA GTPase
593   inhibition organizes contraction during epithelial morphogenesis. *J Cell Biol* **214**, 603-
594   617 (2016).
595 6. Heer, N.C. & Martin, A.C. Tension, contraction and tissue morphogenesis.
596   *Development* **144**, 4249-4260 (2017).
597 7. Pece, S. & Gutkind, J.S. Signaling from E-cadherins to the MAPK pathway by the
598   recruitment and activation of epidermal growth factor receptors upon cell-cell
599   contact formation. *J Biol Chem* **275**, 41227-41233 (2000).
600 8. Fu, C., Arora, A., Engl, W., Sheetz, M. & Viasnoff, V. Cooperative regulation of
601   adherens junction expansion through epidermal growth factor receptor activation. *J
602   Cell Sci* **135** (2022).
603 9. Xu, K.P., Yin, J. & Yu, F.S. SRC-family tyrosine kinases in wound- and ligand-induced
604   epidermal growth factor receptor activation in human corneal epithelial cells. *Invest
605   Ophthalmol Vis Sci* **47**, 2832-2839 (2006).
606 10. Boncompain, G. *et al.* Synchronization of secretory protein traffic in populations of
607   cells. *Nat Methods* **9**, 493-498 (2012).
608 11. Saxena, M. *et al.* EGFR and HER2 activate rigidity sensing only on rigid matrices. *Nat
609   Mater* **16**, 775-781 (2017).
610 12. Antczak, C., Mahida, J.P., Bhinder, B., Calder, P.A. & Djaballah, H. A high-content
611   biosensor-based screen identifies cell-permeable activators and inhibitors of EGFR
612   function: implications in drug discovery. *J Biomol Screen* **17**, 885-899 (2012).
613 13. Hino, N. *et al.* ERK-Mediated Mechanochemical Waves Direct Collective Cell
614   Polarization. *Dev Cell* **53**, 646-660 e648 (2020).
615 14. Hall, A. Rho GTPases and the actin cytoskeleton. *Science* **279**, 509-514 (1998).
616 15. Verma, S. *et al.* A WAVE2-Arp2/3 actin nucleator apparatus supports junctional
617   tension at the epithelial zonula adherens. *Mol Biol Cell* **23**, 4601-4610 (2012).
618 16. Arora, A. *et al.* Cortical ductility governs cell-cell adhesion mechanics. *bioRxiv
619   preprint* (2023).
620 17. Tlili, S. *et al.* Migrating Epithelial Monolayer Flows Like a Maxwell Viscoelastic Liquid.
621   *Phys Rev Lett* **125**, 088102 (2020).
622 18. Honda, H. & Eguchi, G. How much does the cell boundary contract in a monolayered
623   cell sheet? *J Theor Biol* **84**, 575-588 (1980).
624 19. Barton, D.L., Henkes, S., Weijer, C.J. & Sknepnek, R. Active Vertex Model for cell-
625   resolution description of epithelial tissue mechanics. *PLoS Comput Biol* **13**, e1005569
626   (2017).
627 20. Fletcher, A.G., Osterfield, M., Baker, R.E. & Shvartsman, S.Y. Vertex models of
628   epithelial morphogenesis. *Biophys J* **106**, 2291-2304 (2014).
629 21. Alt, S., Ganguly, P. & Salbreux, G. Vertex models: from cell mechanics to tissue
630   morphogenesis. *Philos Trans R Soc Lond B Biol Sci* **372** (2017).
631 22. Lin, S.Z., Merkel, M. & Rupprecht, J.F. Structure and Rheology in Vertex Models
632   under Cell-Shape-Dependent Active Stresses. *Phys Rev Lett* **130**, 058202 (2023).
633 23. Lin, S.Z., Ye, S., Xu, G.K., Li, B. & Feng, X.Q. Dynamic Migration Modes of Collective
634   Cells. *Biophys J* **115**, 1826-1835 (2018).
635 24. Vedula, S.R. *et al.* Emerging modes of collective cell migration induced by
636   geometrical constraints. *Proc Natl Acad Sci U S A* **109**, 12974-12979 (2012).

637   25.   Guilluy, C., Dubash, A.D. & Garcia-Mata, R. Analysis of RhoA and Rho GEF activity in
638   whole cells and the cell nucleus. *Nat Protoc* **6**, 2050-2060 (2011).
639   26.   Azioune, A., Storch, M., Bornens, M., Thery, M. & Piel, M. Simple and rapid process
640   for single cell micro-patterning. *Lab Chip* **9**, 1640-1642 (2009).
641   27.   Yang, R. *et al.* Characterization of mechanical behavior of an epithelial monolayer in
642   response to epidermal growth factor stimulation. *Exp Cell Res* **318**, 521-526 (2012).
643   28.   Stringer, C., Wang, T., Michaelos, M. & Pachitariu, M. Cellpose: a generalist algorithm
644   for cellular segmentation. *Nat Methods* **18**, 100-106 (2021).
645   29.   Ulicna, K., Vallardi, G., Charras, G. & Lowe, A.R. Automated Deep Lineage Tree
646   Analysis Using a Bayesian Single Cell Tracking Approach. *Frontiers in Computer*
647   *Science* **3** (2021).
648   30.   Tlili, S. *et al.* Shaping the zebrafish myotome by intertissue friction and active stress.
649   *Proc Natl Acad Sci U S A* **116**, 25430-25439 (2019).
650   31.   Nakagawa, M., Fukata, M., Yamaga, M., Itoh, N. & Kaibuchi, K. Recruitment and
651   activation of Rac1 by the formation of E-cadherin-mediated cell-cell adhesion sites. *J*
652   *Cell Sci* **114**, 1829-1838 (2001).
653   32.   Kovacs, E.M., Ali, R.G., McCormack, A.J. & Yap, A.S. E-cadherin homophilic ligation
654   directly signals through Rac and phosphatidylinositol 3-kinase to regulate adhesive
655   contacts. *J Biol Chem* **277**, 6708-6718 (2002).
656   33.   Betson, M., Lozano, E., Zhang, J. & Braga, V.M. Rac activation upon cell-cell contact
657   formation is dependent on signaling from the epidermal growth factor receptor. *J*
658   *Biol Chem* **277**, 36962-36969 (2002).
659   34.   Rottner, K., Faix, J., Bogdan, S., Linder, S. & Kerkhoff, E. Actin assembly mechanisms
660   at a glance. *J Cell Sci* **130**, 3427-3435 (2017).
661   35.   Yamazaki, D., Oikawa, T. & Takenawa, T. Rac-WAVE-mediated actin reorganization is
662   required for organization and maintenance of cell-cell adhesion. *J Cell Sci* **120**, 86-
663   100 (2007).
664   36.   Erasmus, J.C., Welsh, N.J. & Braga, V.M. Cooperation of distinct Rac-dependent
665   pathways to stabilise E-cadherin adhesion. *Cell Signal* **27**, 1905-1913 (2015).
666   37.   Lozano, E., Frasa, M.A., Smolarczyk, K., Knaus, U.G. & Braga, V.M. PAK is required for
667   the disruption of E-cadherin adhesion by the small GTPase Rac. *J Cell Sci* **121**, 933-
668   938 (2008).
669
670

671 **Figures**

a Reducing EGFR phosphorylation Impedes cell junction deformation (I).
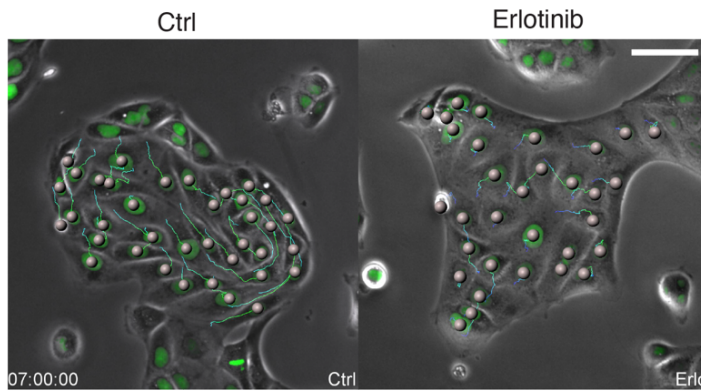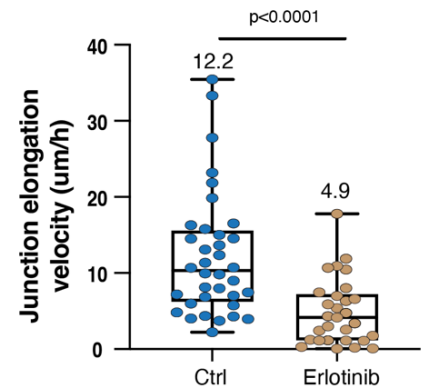
Impeding cell junction deformation reduces EGFR phosphorylation (II).
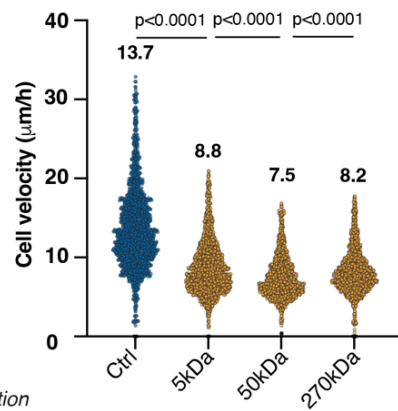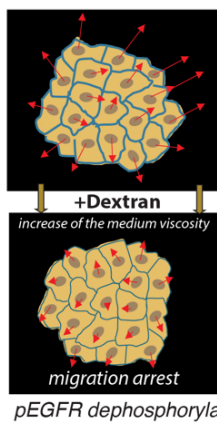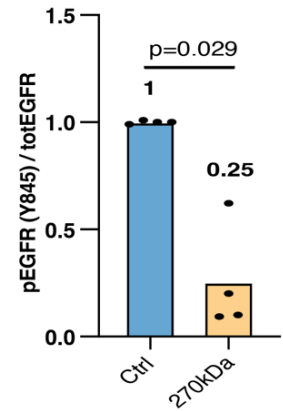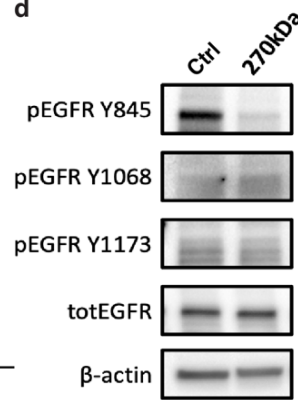
Inducing pEGFR phosphorylation promotes cell junction deformation (III).
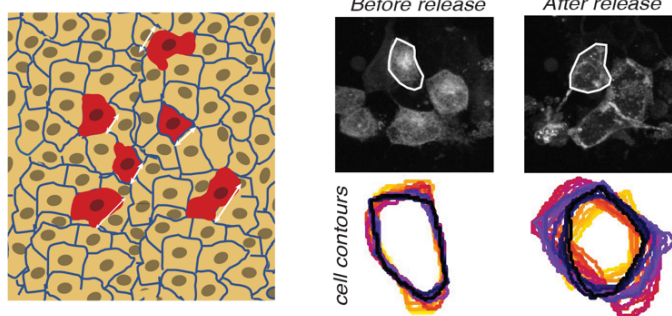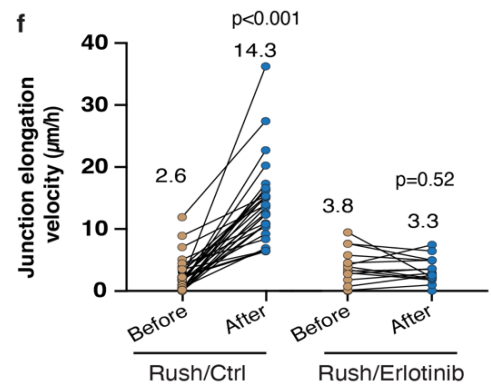
Promoting cell junction deformation induces EGFR phophorylation (IV).

672
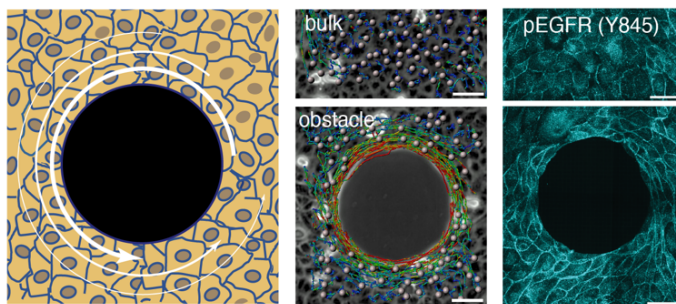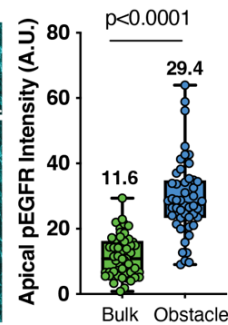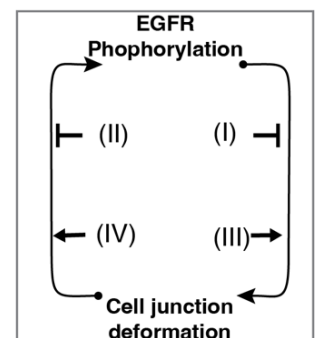
Fig. 1: A positive feedback loop between apical EGFR phosphorylation and cell junction deformation.

a. Representative patches of MDCK cells under control and EGFR-inhibited conditions (Erlotinib at 1μM) including the tracking or individual cell trajectories. Scale bar: 100 μm.

b. Quantification of individual junction elongation velocities in the patches (mean value ± s.d.) n_{Ctrl} = 36 junctions and $n_{Erlotinib}$ = 29 junctions from 3 independent experiments, two-tailed unpaired t-test, p < 0.0001.

c. Schematics of the experiment for cell arrest by dextran addition. Quantification of individual cell migration velocity 10 minutes after adding dextran with various molecular weights (mean value ± s.d. n=1735-1925 cells from 3 independent experiments.)

d. Western Blot and its quantification of EGFR phosphorylated states (Y845) before and after cell arrest from 4 independent experiments, two-tailed unpaired t-test, p = 0.029.

e. Experimental setup schematics (left) and segmented contours quantification (right) of cell mosaically expressing RUSH-EGFR before and after its release from the endoplasmic reticulum.

f. Quantifications of junction elongation velocities upon the release of EGFR, under control and pEGFR-inhibited conditions. $n_{Rush/Ctrl}$ = 28 junctions and $n_{Rush/Erlotinib}$ = 15 junctions from 3 independent experiments, two-tailed paired t-test, $p_{Rush/Ctrl}$ < 0.001, $p_{Rush/Erlotinib}$ = 0.52.

g. Schematics of the physical induction of cell elongation around obstacles (left). Images of cells encircling obstacles and in bulk regions including single cell tracking and apical localization of pEGFR-Y845 by immunostaining. Scale bar: 50 μm.

h. Quantifications of apical pEGFR-Y845 intensity around obstacles (mean value ± s.d. n_{Bulk} = 50 junctions and $n_{Obstacle}$ = 48 junctions from 3 independent experiments, two-tailed unpaired t-test, p<0.0001.)

i. Diagram of a positive feedback loop between apical EGFR phosphorylation and cell junction deformation.

a EGFR phosporylation at junction depends on E-cadherins

b

c
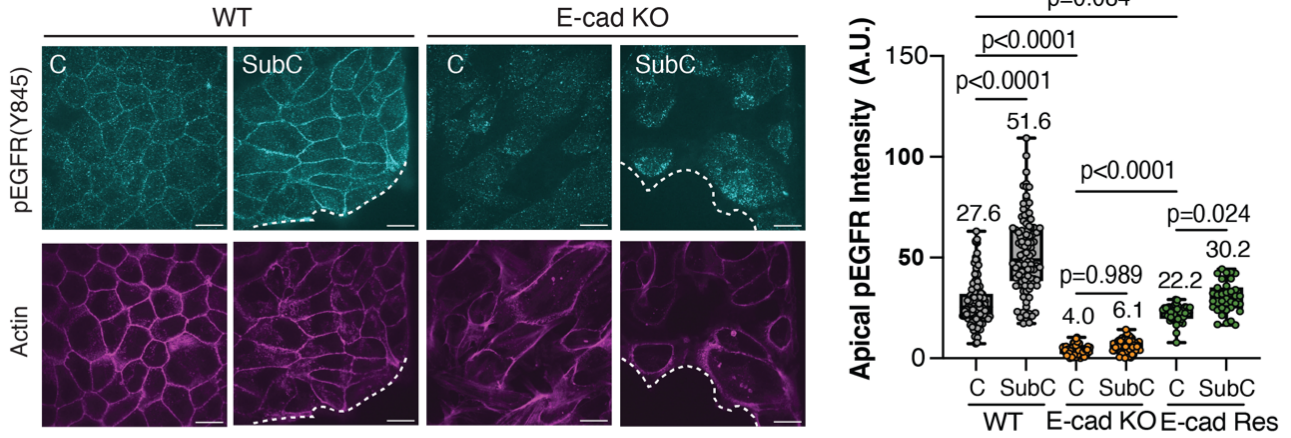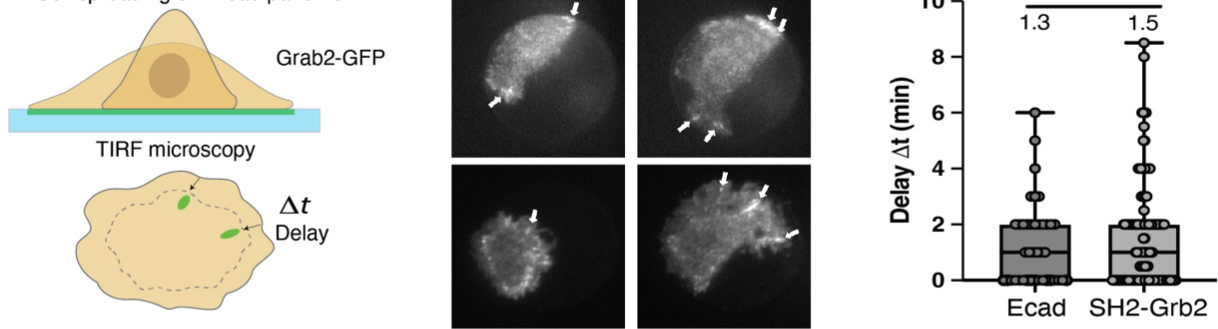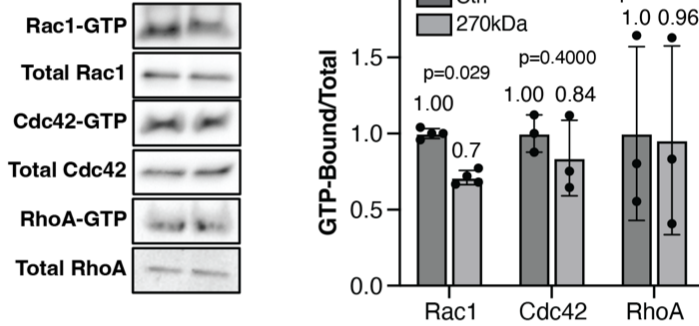
d
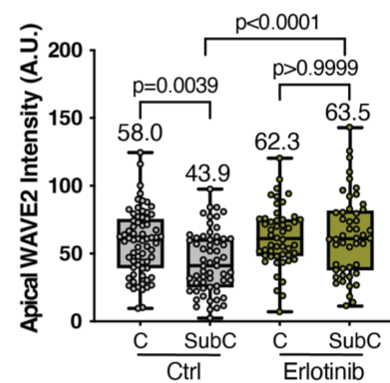
e
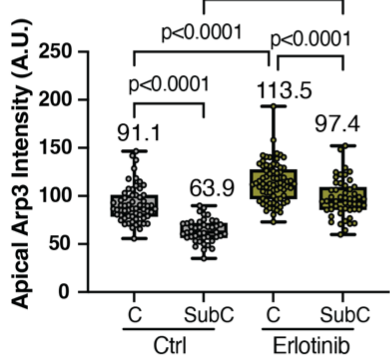
f
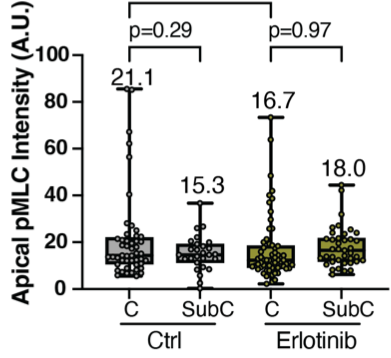
g
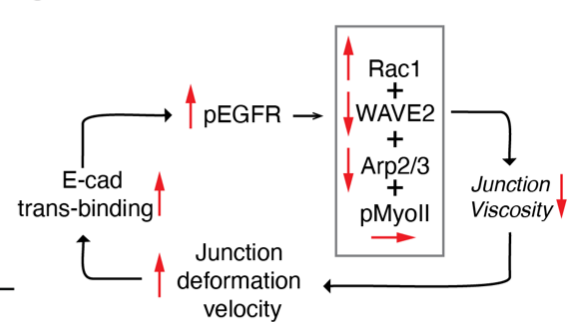
h Rheological properties of junctional actin

i
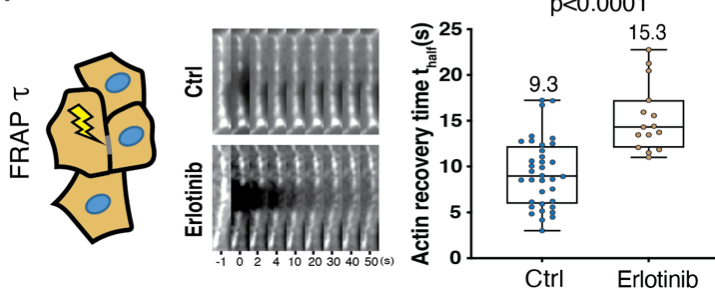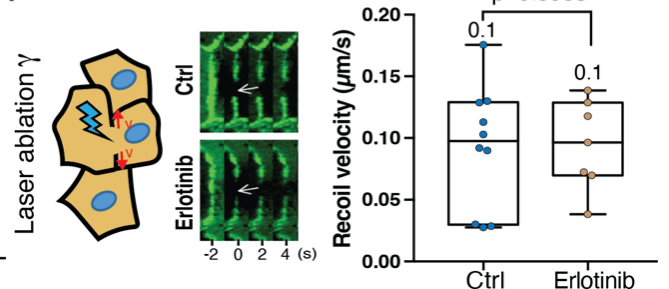
Fig. 2: E-cadherin-dependent phosphorylation of EGFR fine-tunes actin dynamics with minimal impact on cortical tension.

a. Immunostaining of apical pEGFR (Y845) and actin in wild-type (WT) and E-cadherin knock-out (Ecad-KO) MDCKs on confluent (C, left) and sub-confluent (SubC, right) regions. Scale Bar: 20 μm. Quantification of apical pEGFR in WT, Ecad-KO and Ecad-KO-rescued (Ecad-Res) tissues. (WT: n_C = 122 junctions, n_{SubC} = 106 junctions from 4 independent experiments, p < 0.0001; Ecad-KO: n_C = 67 junctions, n_{SubC} = 61 junctions from 3 independent experiments, p = 0.9893; Ecad-Res: n_C = 47 junctions, n_{SubC} = 34 cell junctions from 3 independent experiments, p = 0.0239. Ordinary one-way ANOVA Tukey's test.

b. Schematic (left) and time-lapse imaging (middle) of SH2-Grb2 (tdEOS) and E-cadherin (GFP) localization during cell spreading on E-cadherin-coated patterns. Quantification of the recruitment speed of E-cadherin and SH2-Grb2 (right). n_{Ecad} = 40 cell adhesions and $n_{SH2-Grb2}$ = 132 cell adhesions from 3 independent experiments, two-tailed unpaired t-test, p=0.49.

c. Pull-down assays on Rho family GTPases (Rac1, Cdc42 and RhoA) and quantification of GTP-bound GTPases post cell arrest by dextran. n_{Rac1} = 4 WB, p=0.029, n_{Cdc42} = 3 WB, p=0.4 and n_{RhoA} = 3 WB, p>1, two-tailed unpaired t-test.

d-f. Quantification of apical WAVE2 (**d**), Arp3 (**e**) and pMLC (**f**) under control and EGFR inhibited conditions. Data are the mean value ± s.d. WAVE2: $n_{Ctrl, C}$ = 68 cell junctions, $n_{Ctrl, SubC}$ = 59 cell junctions from 2 independent experiments, $n_{Erlotinib, C}$ = 50 cell junctions, $n_{Erlotinib, SubC}$ = 48 cell junctions from 2 independent experiments; Arp3: $n_{Ctrl, C}$ = 60 cell junctions, $n_{Ctrl, SubC}$ = 43 cell junctions from 2 independent experiments, $n_{Erlotinib, C}$ = 74 cell junctions, $n_{Erlotinib, SubC}$ = 52 cell junctions from 2 independent experiments; pMLC: $n_{Ctrl, C}$ = 49 cell junctions, $n_{Ctrl, SubC}$ = 27 cell junctions from 2 independent experiments, $n_{Erlotinib, C}$ = 62 cell junctions, $n_{Erlotinib, SubC}$ = 39 cell junctions from 2 independent experiments. Ordinary one-way ANOVA Tukey's test.

g. Proposed model of E-cadherin-dependent phosphorylation of EGFR reducing junction viscosity through the regulation of Rac1, WAVE2, Arp2/3, fine-tuning actin dynamics, with minimal impact on cortical tension.

h-i. Experimental schematics and characteristic images of fluorescence recovery after photobleaching (FRAP) (left) and laser ablation (right) experiments on intercellular junctions between GFP-Actin-MDCK cells, Scale Bar: 3 μm. Quantification of fluorescence recovery time (left) and recoil velocities (right) under control and pEGFR-inhibited conditions. FRAP: n_{Ctrl} = 36 cell junctions, $n_{Erlotinib}$ = 15 cell junctions from 3 independent experiments, two-tailed unpaired t-test, p<0.0001; Laser ablation: n_{Ctrl} = 10 cell junctions, $n_{Erlotinib}$ = 7 cell junctions from 2 independent experiments, two-tailed unpaired t-test, p=0.8983.

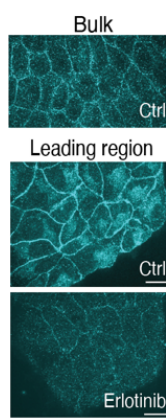**a** Cell migration experiments
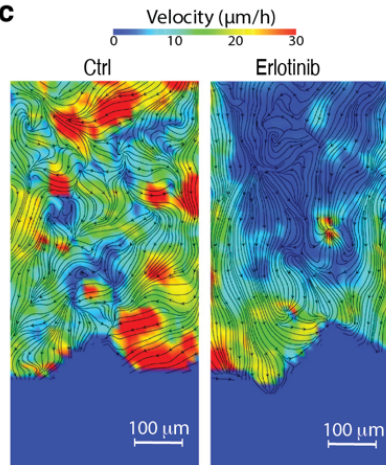
b Bulk / Leading region
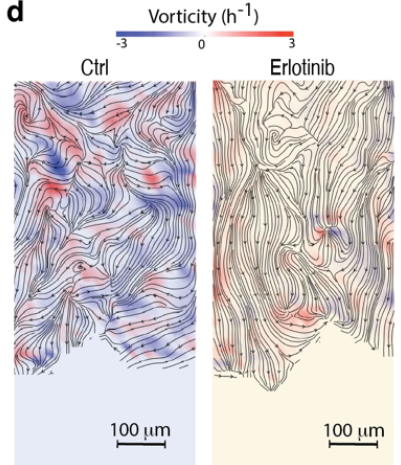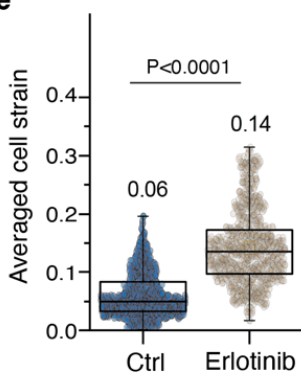
c Velocity (μm/h)

d Vorticity (h⁻¹)

e Averaged cell strain

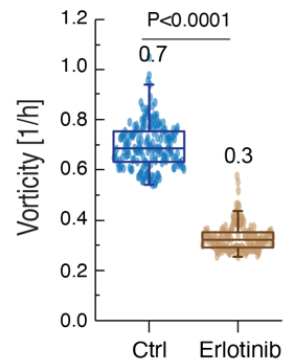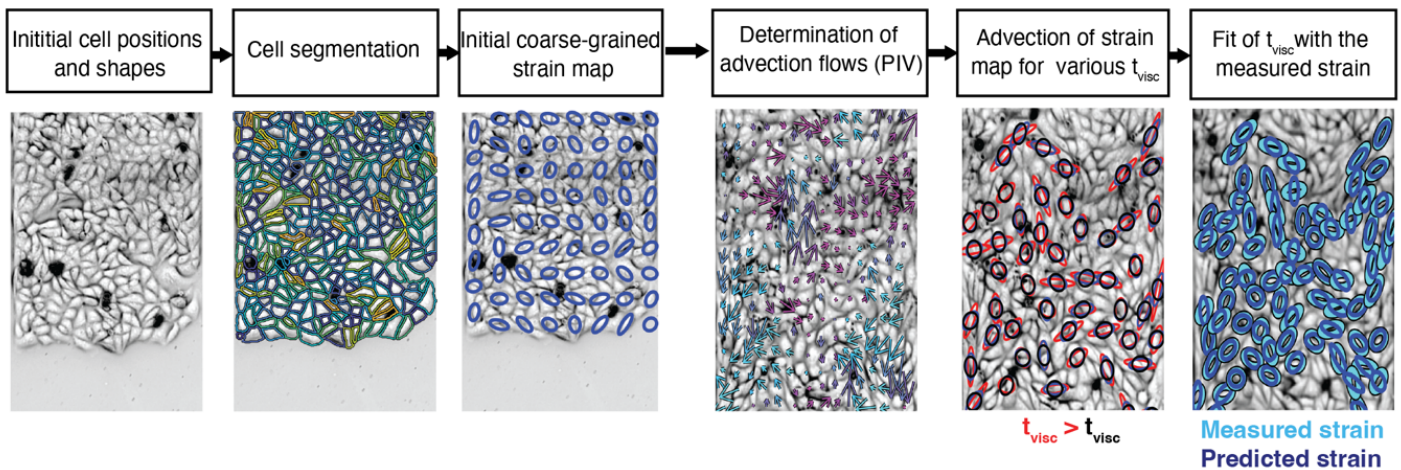**f** Apical pEGFR Intensity (A.U.)

g Velocity [μm/h]
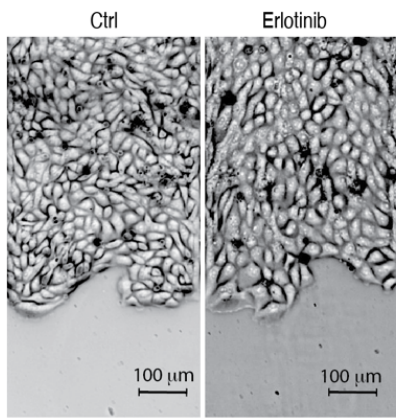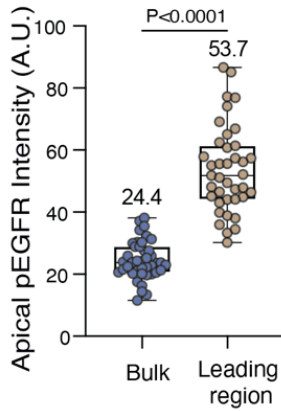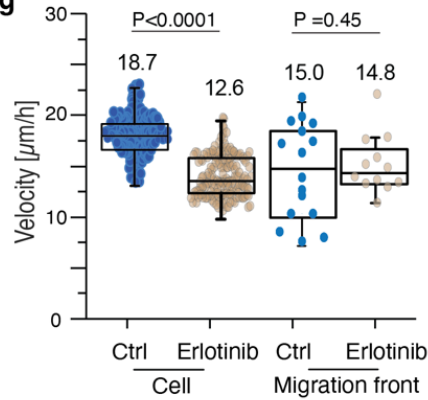
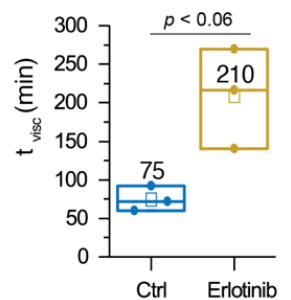**h** Vorticity [1/h]

i Measurement of the dissipative cell relaxation time
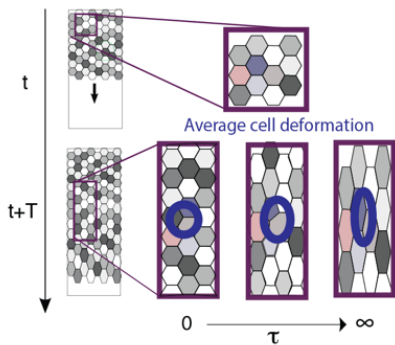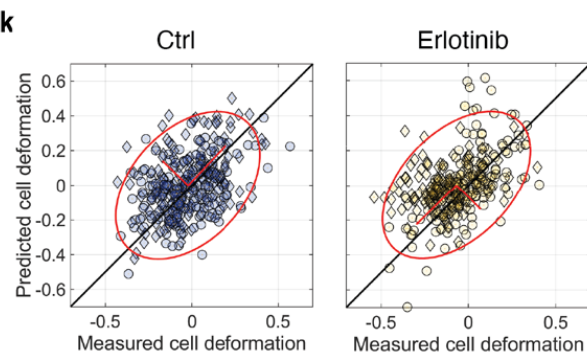
Initital cell positions and shapes → Cell segmentation → Initial coarse-grained strain map → Determination of advection flows (PIV) → Advection of strain map for various t_{visc} → Fit of t_{visc} with the measured strain

j Average cell deformation

k Ctrl / Erlotinib

l t_{visc} (min)

Fig. 3: Phosphorylated EGFR (pEGFR) modulates cell deformability and influences collective migration.

a. Phase-contrast images of MDCK monolayers migrating on fibronectin-coated line patterns under control and pEGFR-inhibited conditions (Erlotinib at 1 μM). Scale Bar: 100 μm. Five independent experiments yielded consistent results.

b. Immunostaining of apical pEGFR(Y845) highlights its localization at cell junctions in bulk and leading regions under control and leading regions under pEGFR-inhibited conditions. Scale Bar: 20 μm. Four independent experiments corroborate these findings.

c-d. Representative velocity (**c**) and vorticity (**d**) profiles with flow line maps, illustrate MDCK monolayer migration under control and pEGFR-inhibited conditions. Scale bar: 100 μm. Three independent experiments yielded consistent results.

e. Quantification of cellular strain states in the monolayer under control and pEGFR-inhibited conditions. n_{Ctrl} = 1060 cells and $n_{Erlotinib}$ = 1060 cells from 3 independent experiments, two-tailed unpaired t-test, p<0.0001.

f. Quantification of apical localization of pEGFR (Y845) at the bulk and leading front region of the monolayer. n_{Bulk} = 42 cell junctions and $n_{leading}$ = 39 cell junctions from 3 independent experiments, two-tailed unpaired t-test, p < 0.0001.

g. Quantification of cell velocity (left) and migration front velocity (right) under control and pEGFR-inhibited conditions. $n_{ctrl, cell}$ = 181 cells, $n_{Erlotinib, cell}$ = 181 cells from 3 independent experiments, p<0.0001; $n_{ctrl, migration front}$ = 16 strips, $n_{Erlotinib, migration front}$ = 12 strips from 3 independent experiments, p=0.45, two-tailed unpaired t-test.

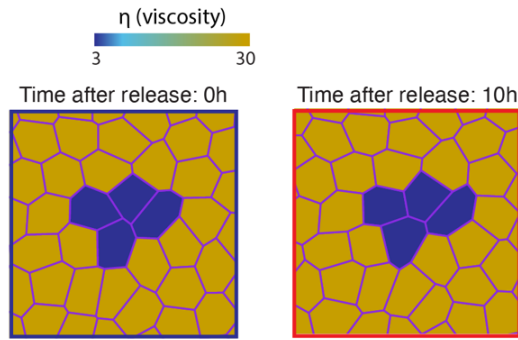**h**. Quantification of spatial correlation in the velocity field under control and pEGFR-inhibited conditions. n_{ctrl}=181 cells, $n_{Erlotinib}$=181 cells from 3 independent experiments, two-tailed unpaired t-test, p<0.0001.

i. Schematic representation of the analysis pipeline to measure the average cell shape relaxation time in a migrating monolayer. Average cell strain profiles along the migration axis are depicted, with bold lines indicating mean values and narrow lines representing standard deviations.
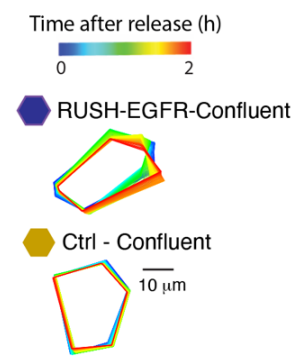
j-k. Correlative plots between measured and advection-based predicted cellular strain for the best fit of the viscoelastic time (t_{visc}) under control and pEGFR-inhibited conditions. Two independent experiments yielded consistent results.

l. Measured viscoelastic time (t_{visc}) under control and pEGFR-inhibited conditions. n_{ctrl}=3 strips, $n_{Erlotinib}$=3 strips from 2 independent experiments, two-tailed unpaired t-test, p<0.06.
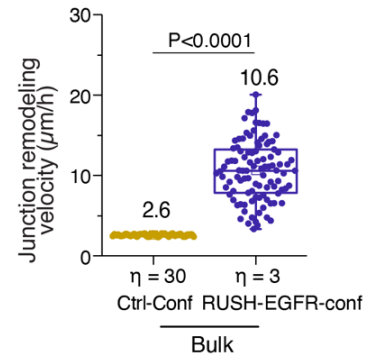
a RUSH-EGFR simulations

η (viscosity)
3 — 30

Time after release: 0h   Time after release: 10h

b

Time after release (h)
0 — 2

RUSH-EGFR-Confluent

Ctrl - Confluent
10 μm

c

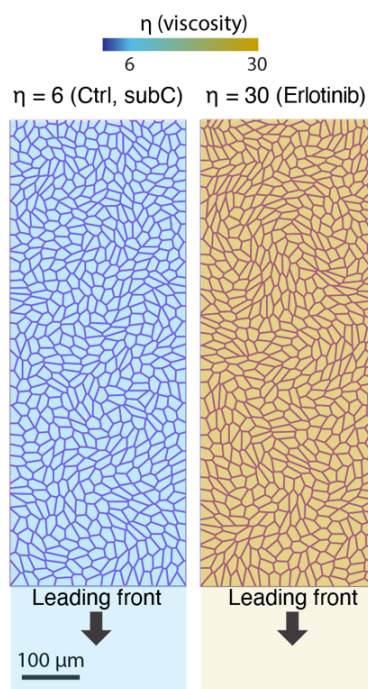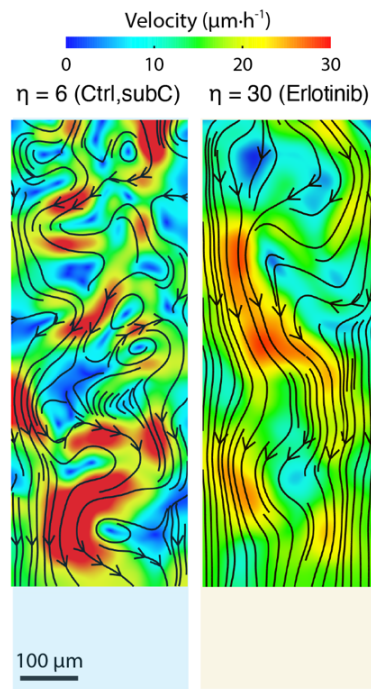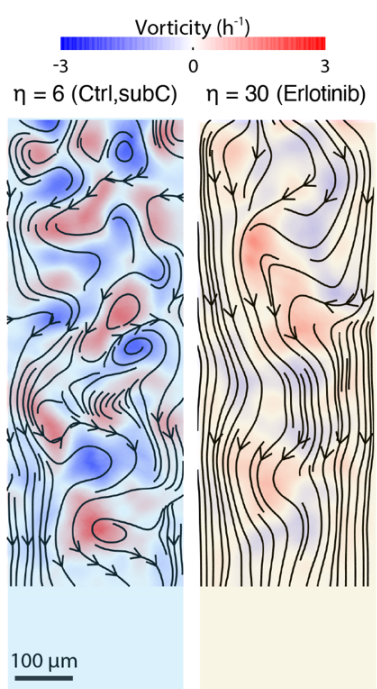Junction remodeling velocity (μm/h)

P<0.0001

10.6
2.6

η = 30   η = 3
Ctrl-Conf   RUSH-EGFR-conf
Bulk

d Cell migration simulations

η (viscosity)
6 — 30

η = 6 (Ctrl, subC)   η = 30 (Erlotinib)

Leading front   Leading front

100 μm

e

Velocity (μm·h⁻¹)
0 10 20 30

η = 6 (Ctrl,subC)   η = 30 (Erlotinib)

100 μm

f

Vorticity (h⁻¹)
-3 0 3

η = 6 (Ctrl,subC)   η = 30 (Erlotinib)

100 μm

g

Cell strain

P<0.0001

0.11
0.04

η = 6   η = 30
(Ctrl)   (Erlotinib)

h

Velocity (μm/h)

P<0.0001

21.2
13.8

η = 6 η = 30   η = 6 η = 30
    Cell   Front

i

Vorticity (h⁻¹)

P<0.0001

0.7
0.34

η = 6   η = 30
(Ctrl)   (Erlotinib)

j

η = 6 (Ctrl)   η = 30 (Erlotinib)

Predicted cell deformation

Measured cell deformation

k

t_{visc} (min)

P = 0.0011

190
70

η = 6 η = 30
(Ctrl) (Erlotinib)

l

	Ctrl subC		Erlotinib	
	Exp	Simul η=6	Exp	Simul η=30
Cell Strain (%)	5	4	10	11
Velocity (μm/h)	18	21	13	14
Vorticity (h⁻¹)	0.9	0.7	0.3	0.3
Corr Length (μm)	110	80	200	150
t_{visc} (min)	75	70	210	190

777

778

Fig. 4: Modeling the impact of viscosity changes on epithelial migration.

a. Simulated cellular arrangement in a vertex model with tension fluctuation, illustrating four low viscosity cells (dark blue, $\eta=3$) within a larger population of normal viscosity cells (orange, $\eta=30$). This models RUSH-EGFR activated cells within a large tissue of inactivated cells.

b. Temporal variation of two representative cell profiles for low viscosity (RUSH-EGFR) cells (top) and control cells (bottom).

c. Quantifications of the cell-cell junction remodeling velocity for control cells and low viscosity (RUSH-EGFR) cells ($\eta=30$ or $\eta=3$, respectively). Conf = Confluent. $n_{Ctrl} = 101$ cell junctions and $n_{RUSH-EGFR} = 101$ cell junctions from simulations, two-tailed unpaired t-test, p<0.0001.

d. Simulated cellular arrangement in a vertex model with $\eta=6$ (light blue) and $\eta=30$ (orange), modelling the control and pEGFR-inhibited (Erlotinib) tissues, in the presence of cellular activity and an imposed uniform front migration speed.

e-f. Velocity (**e**) and, vorticity fields (**f**), both with flow lines (black) for the model of control and pEGFR-inhibited conditions.

g-i. Distribution in the simulated averaged cellular strain (**g**), velocity (displayed together with the imposed front migration speed) (**h**), and vorticity (**i**), under control and pEGFR-inhibited conditions (see **Methods** for averaging procedure). $n_{Ctrl, strain} = 101$ cells and $n_{Erlotinib, strain} = 101$ cells from simulations, two-tailed unpaired t-test, p<0.0001. $n_{Ctrl, velocity} = 100$ cells and $n_{Erlotinib, velocity} = 100$ cells from simulations, two-tailed unpaired t-test, p<0.0001. $n_{Ctrl, vorticity} = 100$ cells and $n_{Erlotinib, vorticity} = 100$ cells from simulations, two-tailed unpaired t-test, p<0.0001.

j. Correlative plots between the measured and advection-based predicted cellular strain for the best fit of the viscoelastic time (t_{visc}) under control ($\eta=6$) and pEGFR-inhibited ($\eta=30$) conditions.

k. Viscoelastic time (t_{visc}) for control ($\eta=6$) and pEGFR-inhibited ($\eta=30$). $n_{Ctrl} = 3$ strips and $n_{Erlotinib} = 3$ strips from simulations, two-tailed unpaired t-test, p=0.0011.

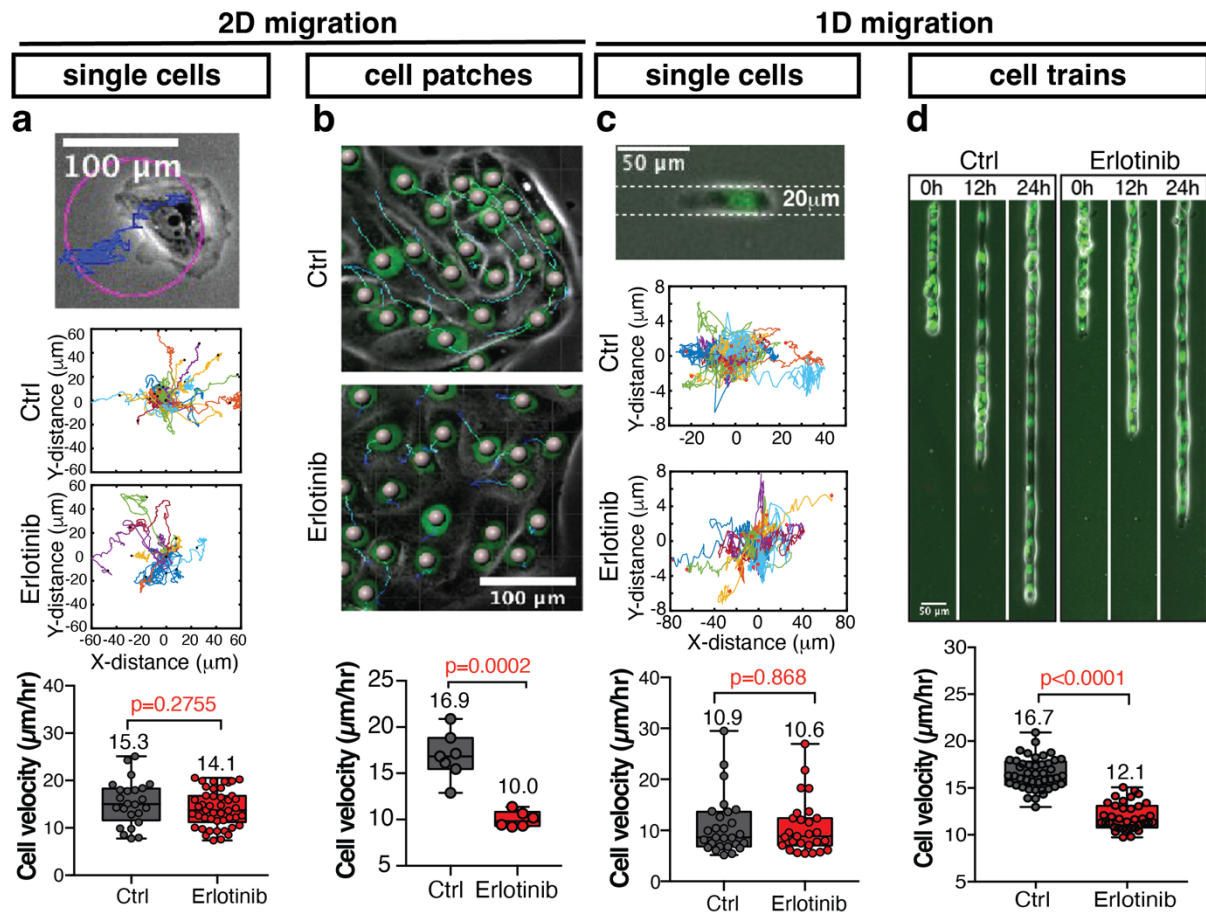**l**. Table summarizing the experimental and simulation results.

806

807

808 **Extended Data Figures**

809

810

811
812
813

814 **Extended Data Fig. 1: Dephosphorylation of EGFR reduces the dynamics of cell junction**
815 **deformation without directly altering cell-substrate interactions.**
816 **a**. Inhibition of EGFR activity does not disrupt single-cell motility in 2D migration.
817 Representative examples of single-cell 2D migration on fibronectin-coated surfaces (top),
818 Scale Bar: 100 µm. Thirty to forty representative nuclear tracks over 12h in cells randomly
819 migrating under Ctrl and pEGFR inhibition conditions (middle). Average speed of single-cell
820 motility from nuclear movement tracks over 12h under Ctrl and pEGFR inhibition conditions
821 (bottom), n_{ctrl} = 24 cells and $n_{Erlotinib}$ = 46 cells from 3 independent experiments, two-tailed
822 unpaired t-test, p=0.2755.
823 **b**. Representative examples of migration of 2D epithelial patches on fibronectin-coated
824 surfaces under Ctrl and pEGFR inhibition conditions (top), Scale Bar: 100 µm. Average speed
825 of cells in patch migration for 12h from nuclear movement tracks under Ctrl and pEGFR
826 inhibition conditions, n_{Ctrl} = 7 cell patches and $n_{Erlotinib}$ = 6 cell patches from 4 different
827 experiments, two-tailed unpaired t-test, p=0.0002.
828 **c**. Inhibition of EGFR activity does not disturb single-cell motility in 1D migration.
829 Representative examples of single-cell migration on 20 µm fibronectin-coated lines (top),
830 Scale Bar: 50 µm. Thirty representative nuclear tracks over 12h in cells migrating on 20 µm
831 line patterns under Ctrl and pEGFR inhibition conditions (middle). Average speed of single-
832 cell motility on 20 µm line patterns from nuclear movement tracks under Ctrl and pEGFR
833 inhibition conditions (bottom), n_{Ctrl} = 27 cells and $n_{Erlotinib}$ = 27 cells from 3 different
834 experiments, two-tailed unpaired t-test, p=0.868.
835 **d**. Representative examples of migration of 1D epithelial trains on 20 µm fibronectin-coated
836 lines under Ctrl and pEGFR inhibition conditions (top), Scale Bar: 50 µm. Average speed of
837 cells in train migration for 24h on 20 µm line patterns from nuclear movement tracks under
838 Ctrl and pEGFR inhibition conditions, n_{Ctrl} = 44 cell trains and $n_{Erlotinib}$ = 36 cell trains from 3
839 different experiments, two-tailed unpaired t-test, p<0.0001.
840

841
842
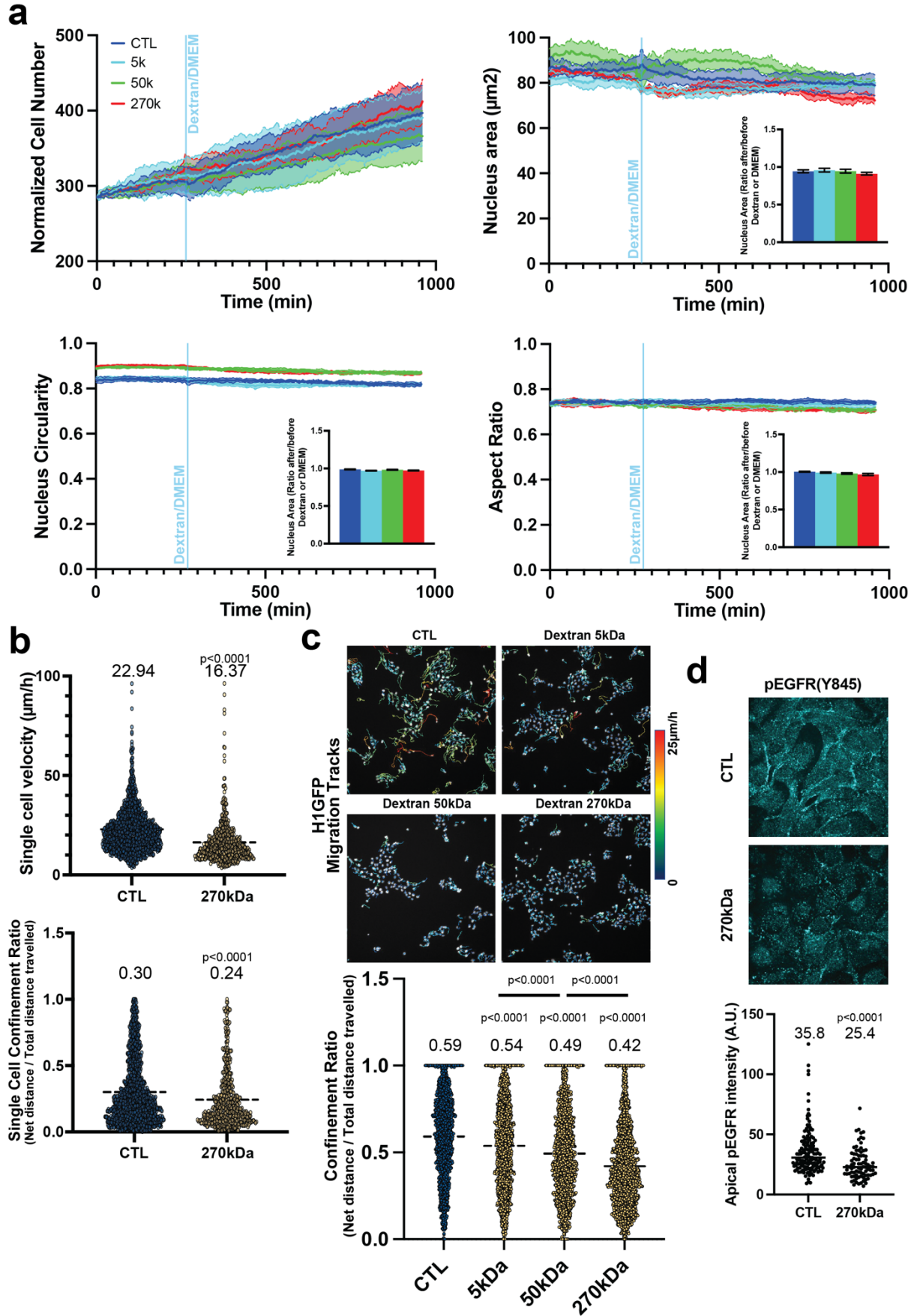
Extended Data Fig. 2: Dextran impact on single and collective cell migration speed and mode without evident signs of osmotic shock.

a. Quantification of cell proliferation (upper left), nucleus area (upper right), circularity (lower left) and aspect ratio (lower right) on cell patches before and after the addition of dextran of the indicated molecular weight. The light blue line indicates the moment of dextran addition. Four independent experiments yielded consistent results.

b. Quantification of single-cells velocity and persistence before and after the addition of 270kDa dextran, n_{Ctrl} = 1217 cells and n_{270kDa} = 543 cells from 3 different experiments, two-tailed unpaired t-test, p<0.0001.

c. Representative images of cell tracking with or without the presence of dextran of the indicated molecular weight (up). Quantification of individual cell persistence within cell patches under control or indicated molecular weight dextran conditions (down), n_{Ctrl} = 1762 cells, n_{5kDa} = 1770 cells, n_{50kDa} = 1424 cells and n_{270kDa} = 1968 cells from 3 different experiments, Ordinary one-way ANOVA Tukey's test, p<0.0001.

d. Confocal images (up) and quantification (down) of pEGFR(Y845) junctional fluorescence intensities under control and 270kDa dextran conditions, n_{Ctrl} = 143 cell junctions and n_{270kDa} = 84 cell junctions from 3 different experiments, two-tailed unpaired t-test, p<0.0001.
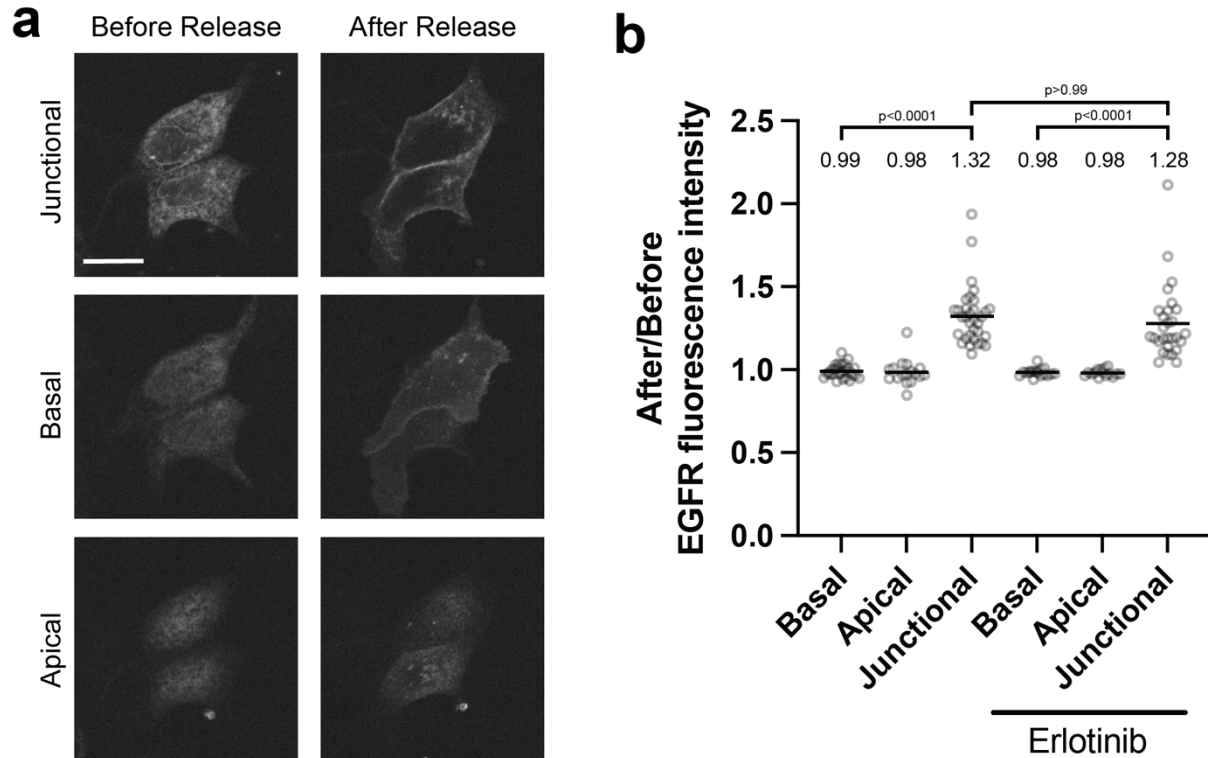
863

864 **Extended Data Fig. 3: EGFR preferentially translocates to cell-cell junction after release from**
865 **the Endoplasmic Reticulum (ER).**
866 **a-b**. Confocal images (**a**) and corresponding quantification (**b**) of EGFR-GFP fluorescence
867 intensities at the junctional, basal and apical side of the cells, both before and after release
868 from the endoplasmic reticulum. Scale Bar: 20 µm. $n_{Ctrl\ Basal}$ = 27 cells, $n_{Ctrl\ Apical}$ = 17 cells, n_{Ctrl}
869 $_{Junctional}$ = 33 cell junctions, $n_{Erlotinib\ Basal}$ = 17 cells, $n_{Erlotinib\ Apical}$ = 15 cells and $n_{Erlotinib\ Junctional}$ = 28
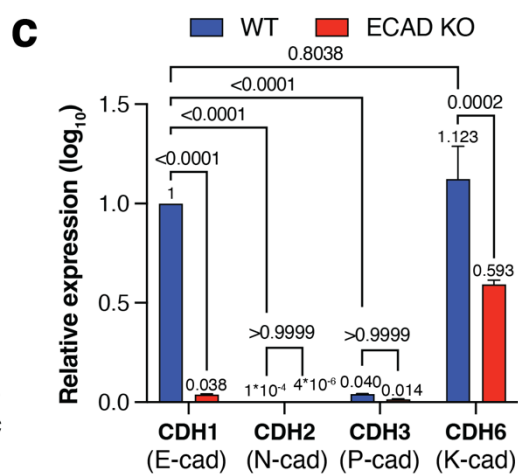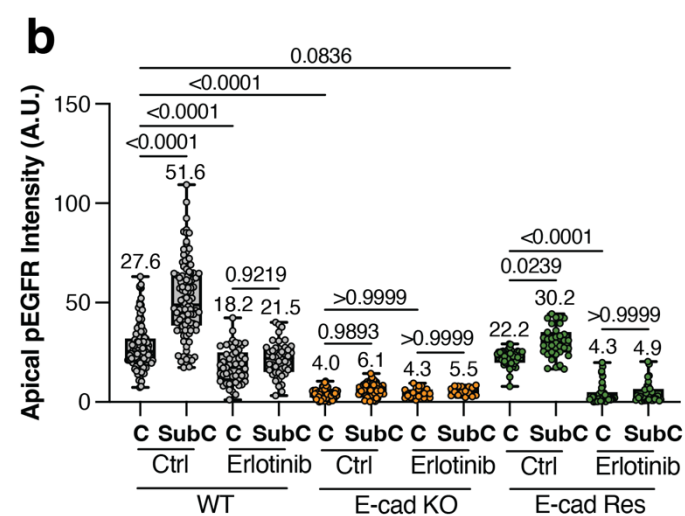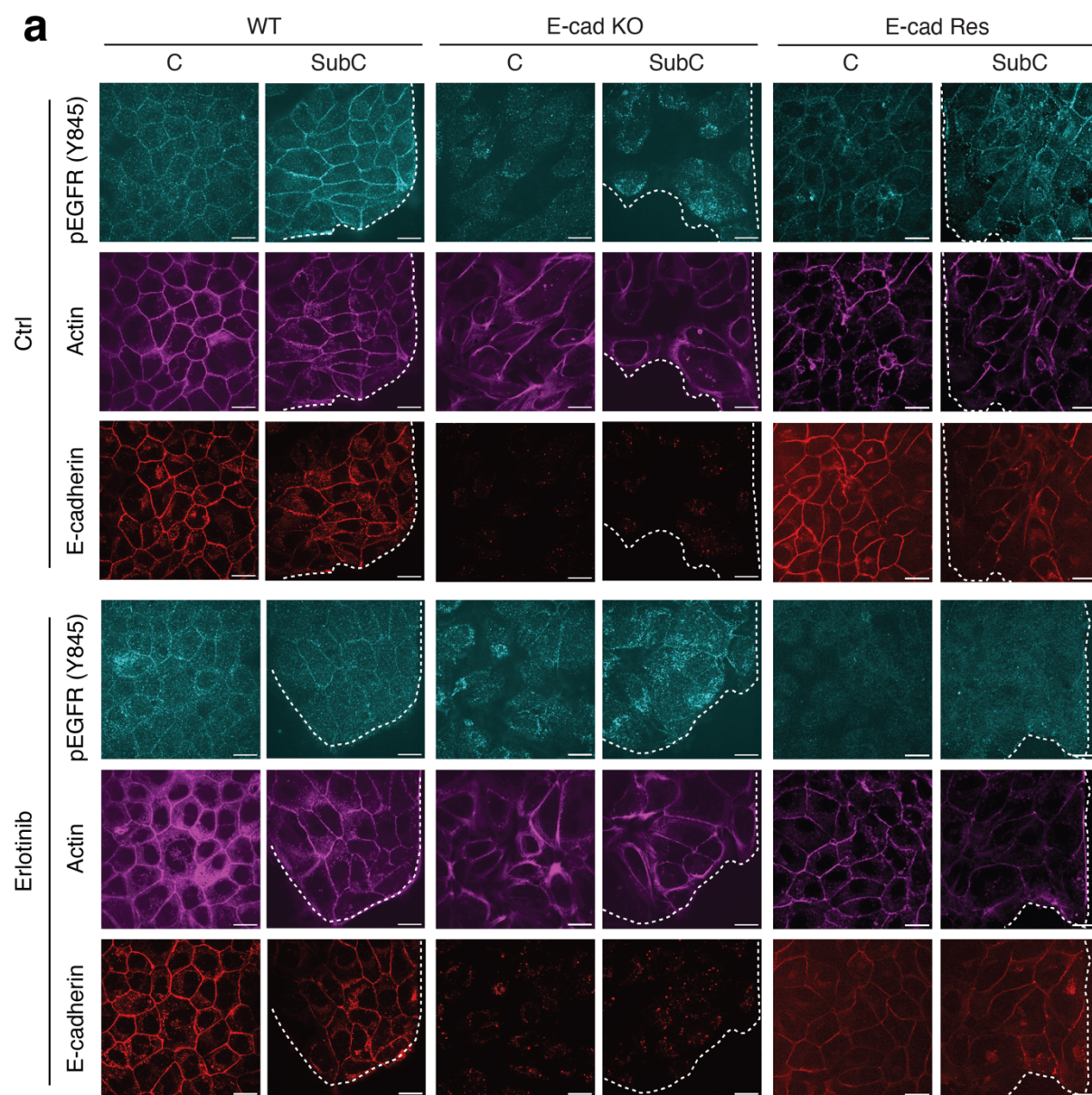870 cell junctions from 3 different experiments, Ordinary one-way ANOVA Tukey's test.
871
872
873

874
875

876 **Extended Data Fig. 4: E-cadherin junctions govern phosphorylation of EGFR (Y845) at the**
877 **apical side of MDCK tissues.**
878 **a**. Immunostaining of pEGFR (Y845), actin and E-cadherin in wild-type (WT), E-cadherin knock-
879 out (Ecad-KO) and Ecad-KO-rescued (Ecad-Res) MDCK cells on the apical side of confluent (C,
880 left) and sub-confluent (SubC, right) regions under control and pEGFR inhibition (Erlotinib)
881 conditions. The white dotted line indicates the leading front of the patches. Scalr Bar: 20 μm.
882 **b**. Quantification of apical pEGFR in WT, Ecad-KO and Ecad-Res MDCK cells. For WT: $n_{Ctrl, C}$ =
883 122 cell junctions, $n_{Ctrl, SubC}$ = 106 cell junctions from 4 different experiments, $n_{Erlotinib, C}$ = 51
884 cell junctions, $n_{Erlotinib, SubC}$ = 44 cell junctions from 3 different experiments; For Ecad-KO: $n_{Ctrl,}$
885 $_{C}$ = 67 cell junctions, $n_{Ctrl, SubC}$ = 61 cell junctions from 3 different experiments, $n_{Erlotinib, C}$ = 24
886 cell junctions, $n_{Erlotinib, SubC}$ = 16 cell junctions from 3 different experiments; For Ecad-Res: $n_{Ctrl,}$
887 $_{C}$ = 47 cell junctions, $n_{Ctrl, SubC}$ = 34 cell junctions from 3 different experiments, $n_{Erlotinib, C}$ = 41
888 cell junctions, $n_{Erlotinib, SubC}$ = 32 cell junctions from 3 different experiments, Ordinary one-way
889 ANOVA Tukey's test.
890 **c**. RT-qPCR results showing the relative expression of CDH1 (E-cad), CDH2 (N-cad), CDH3 (P-
891 cad) and CDH6 (K-cad) in WT and Ecad-KO MDCK cells from 3 different experiments.
892
893

894
895
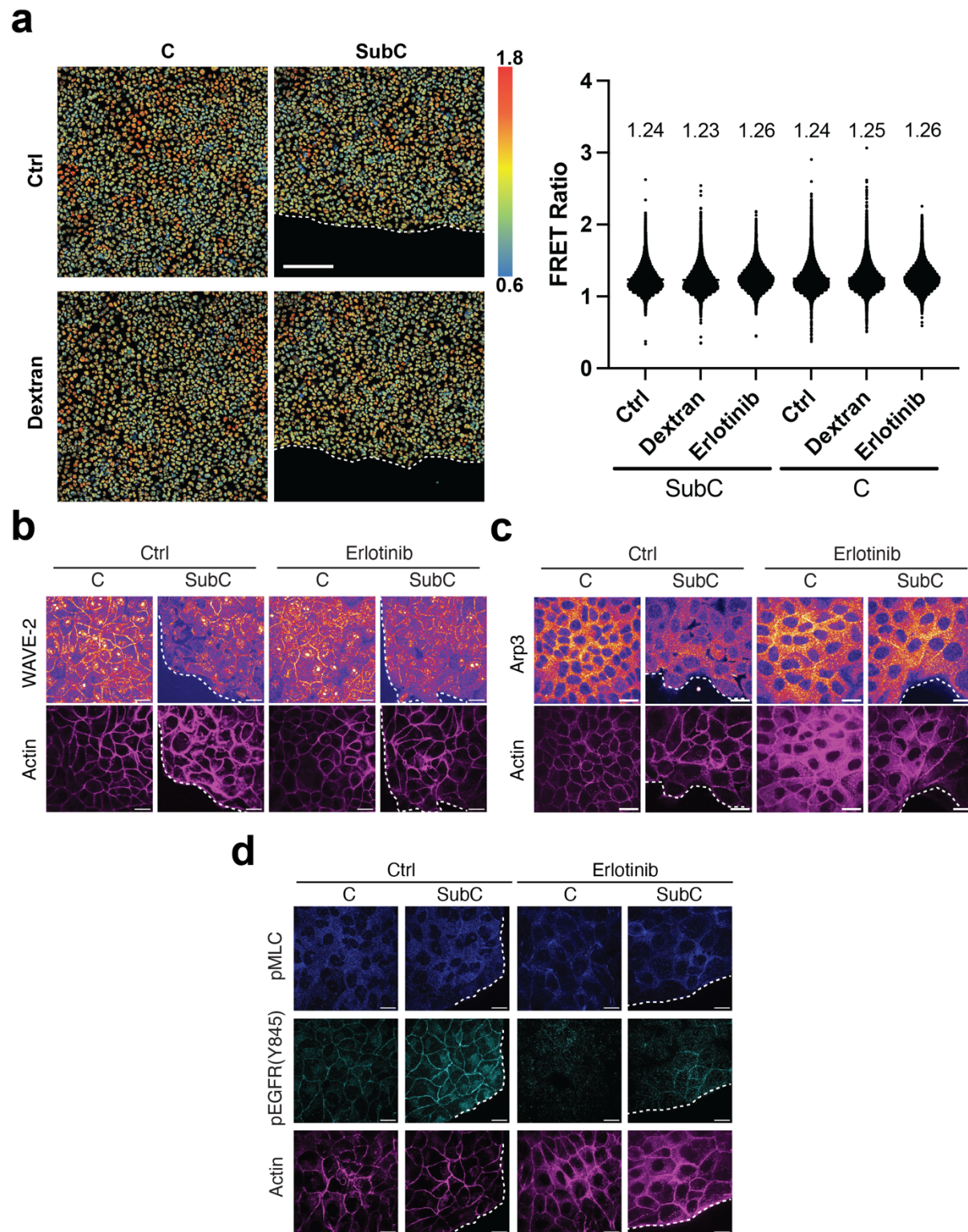
**Extended Data Fig. 5: Molecular components underlying EGFR phosphorylation in response to cell junction deformation.**

a. Representative images and corresponding quantification of FRET Ratio in confluent (C, left) and sub-confluent (SubC, right) regions of migrating MDCK monolayers, with or without EGFR inhibition (Erlotinib), $n_{Ctrl, SubC}$ = 27014 cells, $n_{Dextran, SubC}$ = 27766 cells, $n_{Erlotinib, SubC}$ = 15316 cells, $n_{Ctrl, C}$ = 43852 cells, $n_{Dextran, C}$ = 43079 cells and $n_{Erlotinib, C}$ = 27305 cells from 3 independent experiments. Scale Bar: 200 μm.

b-c. Immunostaining of WAVE-2 and actin (**b**), Arp3 and actin (**c**) on the apical side of confluent (C, left) and sub-confluent (SubC, right) regions under Control and pEGFR inhibition (Erlotinib) conditions. Scale Bar: 20 μm. Two independent experiments yielded consistent results.

d. Immunostaining of pMLC, pEGFR (Y845) and actin on the apical side of confluent (C, left) and sub-confluent (SubC, right) regions under control and pEGFR inhibition (Erlotinib) conditions. Scale Bar: 20 μm. Two independent experiments yielded consistent results.

911
912
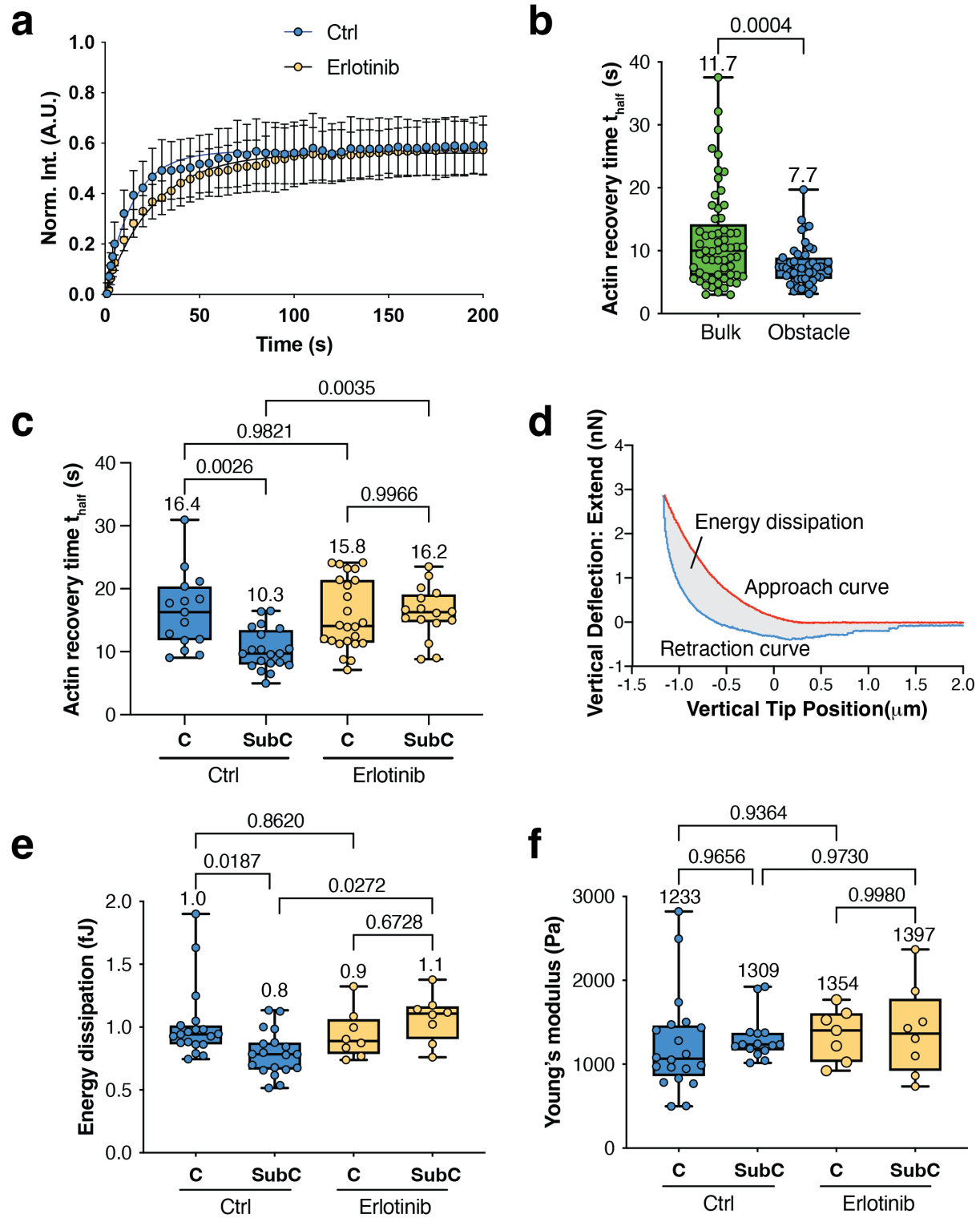
Extended Data Fig. 6: Regulation of actin dynamics and junctional viscoelastic properties by EGFR phosphorylation without impact on junctional tension.

a. Fluorescence Recovery After Photobleaching (FRAP) experiments of actin were conducted at the apical regions of cell-cell junctions under both control and pEGFR inhibition (Erlotinib) conditions. The data were normalized and fitted with best-fit curves.

b. Actin dynamics were assessed in cells encircling obstacles and in bulk regions. n_{Bulk} = 61 cell junctions and $n_{Obstacle}$ = 47 cell junctions from 3 independent experiments, two-tailed unpaired t-test, p=0.0004.

c. Measurements of actin dynamics in migrating MDCK monolayers were performed in both confluent (C, left) and sub-confluent (SubC, right) regions under control and pEGFR inhibition (Erlotinib) conditions. $n_{Ctrl, C}$ = 15 cell junctions, $n_{Ctrl, SubC}$ = 20 cell junctions from 2 independent experiments, $n_{Erlotinib, C}$ = 24 cell junctions, $n_{Erlotinib, SubC}$ = 16 cell junctions from 3 independent experiments, Ordinary one-way ANOVA Tukey's test.

d. Typical force-displacement curves from Atomic Force Microscopy (AFM) force measurements of MDCK monolayers. The area enclosed between the approach and retraction curves, corresponds to energy dissipation.

e-f. Measurements of energy dissipation (**e**) and Young's modulus (**f**) of migrating MDCK monolayers in confluent (C, left) and sub-confluent (SubC, right) regions under control and pEGFR inhibition (Erlotinib) conditions. For energy dissipation: $n_{Ctrl, C}$ = 19 cell junctions, $n_{Ctrl, SubC}$ = 19 cell junctions from 3 independent experiments, $n_{Erlotinib, C}$ = 8 cell junctions, $n_{Erlotinib, SubC}$ = 8 cell junctions from 3 independent experiments, Ordinary one-way ANOVA Tukey's test. For Young's modulus: $n_{Ctrl, C}$ = 20 cell junctions, $n_{Ctrl, SubC}$ = 15 cell junctions from 3 independent experiments, $n_{Erlotinib, C}$ = 7 cell junctions, $n_{Erlotinib, SubC}$ = 8 cell junctions from 3 independent experiments, Ordinary one-way ANOVA Tukey's test.

Supplementary Discussion:

E-Cadherin - EGFR - Rac1 - Wave2 - Arp2/3 interplay and relevance at cell-cell junctions.

In this study, we elucidated a molecular signaling pathway that plays a crucial role in regulating the viscosity of intercellular junctions. Our findings demonstrate that the trans binding of E-cadherin within highly dynamic cell-cell junctions triggers the activation of EGFR and Rac1, aligning with previous research[7, 31-33]. Rac1 has been well-established to play a major role in Wave2 complex recruitment and activation[34]. Specifically, E-cadherins activate Rac1 at the cell-cell junction, contributing to junction stabilization through Wave2[35, 36].

Contrary to existing studies conducted on highly confluent monolayers characterized by mature contacts and non-dynamic cell-cell junctions, our investigation focuses on sub-confluent patches exhibiting elevated apical pEGFR and Rac1-GTP levels. In our unique context of high dynamics, we proposed that the signaling pathways and molecular actors may differ. Notably, Rac1 activation, which has been linked to E-cadherin adhesion disruptions[37], could potentially contribute to the rapid turnover of E-cadherin adhesions in highly dynamic cell-cell junctions, thereby hindering Wave2 recruitment for junction stabilization.

Alternatively, we hypothesize that the impact of pEGFR at the junction is non-local, coupling with recruitment at the basal part of cells and creating competition with the junctional pool. Unfortunately, due to limitations in the available imaging techniques, we were unable to discern the cortex bound to the cytoplasmic fraction. Consequently, while our paper establishes a correlation between the recruitment levels of various proteins, we refrain from asserting a direct causal link.

Captions of the Supplementary videos.

Supplementary Video 1:
Cell-cell reorganization in representative patches of MDCK-H1-GFP cells under control and pEGFR-inhibited (Erlotinib at 1μM) conditions recorded at 12 frames/hour. Scale Bar: 100μm.

Supplementary Video 2:
Cell patches migration of MDCK-H1-GFP cells with or without dextran addition recorded at 12 frames/hour. Scale Bar: 100μm.

Supplementary Video 3:
MDCK-WT monolayers with mosaic expression of RUSH-EGFR-GFP. Junction elongation before and after addition of biotin and subsequent release of EGFR from the endoplasmic reticulum under control and pEGFR-inhibited (Erlotinib at 1μM) conditions recorded at 12 frames/hour. Scale Bar: 20μm.

Supplementary Video 4:
Cells encircling obstacles and in bulk regions under control and pEGFR-inhibited (Erlotinib at 1μM) conditions recorded at 15 frames/hour. Scale Bar: 50μm.

Supplementary Video 5:
Cells migrating on 400 μm width line strips under control and pEGFR-inhibited (Erlotinib at 1μM) conditions recorded at 15 frames/hour. Scale Bar: 100μm.

Supplementary Video 6:
The vorticity of the collective flow for the migrating cells under control and pEGFR-inhibited (Erlotinib at 1μM) conditions recorded at 15 frames/hour.

Supplementary Video 7:
Vertex-model simulations under control (η=6) and pEGFR-inhibited (Erlotinib at 1μM) (η=30) conditions. Other parameters see Supplementary Table II.